Gaute Holst Aasland

Synthesis of Silica Aerogels with Single-Site Iron for Heterogeneous Catalysis

Master's thesis in Chemistry
Supervisor: Karina Mathisen & Karsten Granlund Kirste
May 2019

Master's thesis

NTNU
Norwegian University of Science and Technology
Faculty of Natural Sciences
Department of Chemistry

NTNU
Norwegian University of
Science and Technology

Gaute Holst Aasland

Synthesis of Silica Aerogels with Single-Site Iron for Heterogeneous Catalysis

Master's thesis in Chemistry
Supervisor: Karina Mathisen & Karsten Granlund Kirste
May 2019

Norwegian University of Science and Technology
Faculty of Natural Sciences
Department of Chemistry

NTNU
Norwegian University of
Science and Technology

Acknowledgements

This work has been carried out at the Department of Chemistry (IKJ) at the Norwegian University of Science and Technology (NTNU) in Trondheim.

First off, I would like to thank my supervisor Karina Mathisen and co-supervisor Karsten Granlund Kirste. This work would not have been possible without your supervision, assistance and valuable feedback. I would also like to extend my deepest gratitude to the entirety of the structural chemistry group for providing guidance, feedback and discussion whenever needed, as well as very welcome social gatherings, fun trips, and delicious cakes. A special thanks especially to Guro, Daniel, Tina, and Stian, as well as fellow graduating master students Anders, Sigurd, and Caren.

Secondly, I would like to recognize the helpful individuals who assisted with all the characterization instruments. I would like to thank Kristin Høydalsvik Wells and Silje Marie Dale for the support with the XRD apparatus, Elin Harboe Albertsen for always being ready to help during BET analysis, Syverin Lierhagen for running the ICP-MS samples, and Thor Bernt Melø for setting up and letting me use his work space for UV-vis analysis. Your help is deeply appreciated.

Lastly, my old and new classmates deserves to be mentioned. What a great time we have had! A salute is also extended to the casts of Critical Role and High Rollers for providing endless hours of live-streamed entertainment when needed. I am forever grateful for my family and friends. This has not been a small workload, and as some crucial moments of my life have also transpired during these last two years, it has made for an uneasy road. You being there for me has given me more encouragement than anything. The myriad of good times have even made me forget all about this massive piece of work at times.

Thank you!

Sammendrag

Jern ble inkorporert i silika aerogeler laget med "waterglass" silika-forløper. Co-forløper (CP) syntesemetoden ble brukt i kombinasjon med en mer økonomisk tørking ved lavere temperatur og trykk (APD). En ny metode med inert nitrogen-atmosfære ble også testet ut. Ulike jernmengder og fire ulike jernforløpere ble brukt i forsøket på å introdusere jernet i såkalte "single-sites". Aerogelprøvene ble karakterisert med røntgendiffraksjon (XRD), nitrogen-sorpsjon (BET og BJH), induktivt koblet plasma massespektrometri (ICP-MS), og ultrafiolett-synlig (UV-vis) spektroskopi.

Lavt jerninnhold ($\leq$ 2.5 wt% Fe) virket nødvendig for å inkorporere jernet kun som "single-sites" i silika-nettverket, og mulig tetraedrisk koordinasjon av jernet ble antydet av absorpsjonspektrene. Jern diklorid virket mindre egnet enn de andre jernforløperene grunnet økt dannelse av jernoksid i prøvene. XRD, BET og BJH indikerte at dopingen med jern forårsaket endringer i porøsiteten sammenlignet med udopet silikagel, vist av økt porøsitet for moderate jernmengder ($\leq$ 5 wt% Fe) og redusert porøsitet for større mengder (5-14 wt% Fe). Den termiske stabiliteten til jerndopede aerogeler var ubestemt, ettersom varmebehandling ved 450 °C muligens favoriserte dannelse og krystallisering av jernoksidpartikler.

Abstract

Iron was incorporated into silica aerogels made using a waterglass precursor and applying the co-precursor (CP) approach in combination with the ambient pressure drying (APD) method. A novel approach applying an inert nitrogen atmosphere was also used. Varied iron content and four different iron precursors were used in the attempt to incorporate the guest metal into so-called single-sites. The aerogel samples were characterized by X-ray powder diffraction (XRD), nitrogen physisorption (BET and BJH), inductively coupled plasma mass spectrometry (ICP-MS), and ultraviolet-visible (UV-vis) spectroscopy.

Low iron loadings ($\leq$ 2.5 wt% Fe) appeared necessary to incorporate iron only as single-sites, and tetrahedral coordination of the iron sites were likely, as inferred from absorption spectra. Moreover, ferrous chloride appeared unsuitable for this synthesis due to increased oxide formation compared to the other three precursors. XRD and nitrogen physisorption indicated that introduction of iron into the aerogel led to changes in the porosity compared with the plain silica gel, shown by increased porosity for moderate loadings ($\leq$ 5 wt% Fe) and decreased porosity for larger loadings (5-14 wt% Fe). The thermal stability of the Fe-modified gels was inconclusive, as annealing at 450 °C possibly favored the formation and crystallization of iron oxide particles.

Abbreviations

APD	Ambient pressure drying
BET	Brunauer-Emmett-Teller
BJH	Barret-Joyner-Halenda
CP	Co-precursor
CT	Charge transfer
EPR	Electron paramagnetic resonance
EXAFS	Extended x-ray absorption fine structure
HMDS	Hexamethyldisilizane
HMDSO	Hexamethyldisiloxane
iCP	Co-precursor with inert atmosphere
ICP-MS	Inductively coupled plasma mass spectrometry
LMCT	Ligand-to-metal charge transfer
MLCT	Metal-to-ligand charge transfer

MMO	Methane monooxygenase
MO	Molecular orbital
MS	Mass spectrometry
PSD	Pore size distribution
RLCA	Reaction limited cluster aggregation
RLMC	Reaction limited monomer-cluster growth
SCD	Supercritical drying
SCR	Selective catalytic reduction
SD	Surface derivatization
SSHC	Single-site heterogeneous catalyst
TMI	Transition metal ion
TMS	Trimethylsilyl
UV-vis	Ultraviolet-visible
XAS	X-ray absorption spectroscopy
XRD	X-ray (Powder) diffraction

Contents

Chapter 1

Introduction

New materials are constantly being developed, and have had an enormous impact on human history. Historic eras have even been named after the defining materials of that age. This includes the stone age, the bronze age, the iron age, and possibly a "plastic age" we are currently residing in.[1] Not a century ago, Kistler was the first to discover and synthesize aerogels,[2] a group of porous materials derived from wet gels whose structure are almost completely made up of air (up to 99%).[3] In the following years, but especially in the more recent decades, aerogels have attracted a lot of attention due to their unique combination of properties, such as very high surface area (up to $1200\,\mathrm{m^2\,g^{-1}}$), low density (as low as $0.003\,\mathrm{g\,cm^{-3}}$), and low thermal conductivity (down to $0.017\,\mathrm{W\,m^{-1}\,K^{-1}}$).[3] In addition, aerogels are made using sol-gel processing, which provides a viable and versatile synthesis in which the material can be tailored for specific purposes.[4,5] The inexpensive silica precursor known as waterglass, as well as a less demanding drying process which does not require high temperatures and pressures, have

also contributed to making preparation of aerogels more economical in recent years.[6] Their interesting properties combined with this versatile synthesis make aerogels favorable for a number of applications, one of them being as catalyst materials.[7,8]

Iron is cheap and abundant (being the fourth most common element in the Earth's crust),[9] and has been shown to be an active catalyst for a number of reactions. Most prominent is the selective catalytic reduction (SCR) of NO_x and the conversion of methane.[10–12] Methane is known for its inherent lack of reactivity due to four strong C–H bonds, but the enzyme methane monooxygenase (MMO), which contains an active iron site, is capable of breaking these bonds at ambient temperatures.[11] An efficient direct conversion of methane is highly sought after, as methane in natural gas will become the main source of hydrocarbons for fuels and chemicals in the future. For now, the indirect route of methane conversion via syngas (H_2 + CO) is both expensive and energy intensive.[13] Because of this, heterogeneous catalysts which can mimic the function of MMO have been pursued for some time.[12,14–17] This includes catalysts based on porous materials such as zeolites and aerogels.

Recently, attention has been drawn to single-site heterogeneous catalysts (SSHC), since they provide good accessibility and have been associated with higher catalytic efficiency.[12,18] This warrants more attempts at incorporation of single-sites in porous materials to see if a new generation of catalysts can be made. Previous works have addressed the introduction of single-site guest metals into aerogels via more economically viable synthesis routes.[19] In 2011, Kristiansen et al. were the first to successfully synthesize aerogels this way with single-site copper incorporated. With 67% conversion at 450 °C, this material displayed prominent catalytic performance towards the SCR of NO_x.[20,21] Later studies have focused on similar introduction of other

metals into the aerogel matrix through inexpensive preparation, in particular copper, molybdenum, rhenium and iron.[22–24] In these works, a varying degree of success have been reported. For the prior work with iron, Kristoffersen worked exclusively with iron nitrate and looked at the species formed using spectroscopic techniques.[24] Iron speciation in aerogels and silicates was also given some attention through the 1990's and early 2000's, with a variety of iron species being reported to appear in the materials.[25–27] The main difference now from these earlier attempts is the improved synthesis route, which provides a less dangerous and more economically suitable option.

As such, the aim of this thesis was to synthesize aerogel using inexpensive precursors and the ambient pressure drying (APD) method, with iron incorporated into single-sites. Prepared gels have been characterized using standard characterization methods, including X-ray powder diffraction (XRD), nitrogen physisorption (BET and BJH), inductively coupled plasma mass spectrometry (ICP-MS) and ultraviolet-visible (UV-vis) spectroscopy. The intended purpose of the Fe-modified aerogels was the possible application as catalysts for methane conversion or other reactions, however catalytic testing was beyond the scope of this project.

Chapter 2

Theory

2.1 Silica Aerogels

Aerogels are a diverse class of solid inorganic materials that are derived from gels, but in which the liquid component of the traditional wet gel has been replaced by a gas.[28] Historically, the first aerogels were made in the 1930's by Kistler,[2] but many advances in the synthesis methods have developed in the more recent decades. The ones first made and the most common aerogels are silica (SiO_2) based, which is why the term aerogel is often used to refer specifically to this kind. However, there are a variety of other aerogels based on inorganic and other materials, such as alumina (Al_2O_3), zirconia (ZrO_2), titania (TiO_2), and carbon (C).[29–32]

Aerogels are composed of an amorphous and porous network of interconnected silica particles with a structure that can resemble a string

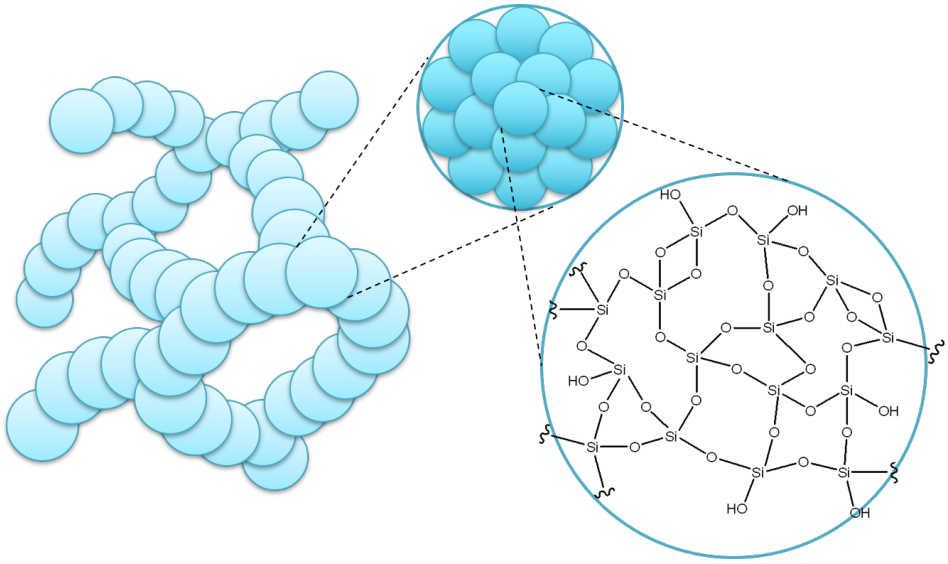

Figure 2.1: The structure of silica aerogel. Silicon and oxygen form the primary silica particles, which again form secondary particles arranged in a random network.

of pearls, as can be seen in Figure (2.1). The primary particles are typically in the range of 1-3 nm, and cluster together to form the secondary particles which can be up to 10 nm wide.[3] The pore structure of aerogels is characterized by well-accessible and random pores within the micro- and the mesoporous regimes, in which micropores have a diameter smaller than 2 nm (20 Å) while mesopores are in the range of 2-50 nm (20-500 Å).[33]

Silica aerogels, as well as other aerogels, exhibit an interesting combination of properties such as high surface area (up to 1200 $m^2\,g^{-1}$), high porosity (up to 99%), low density (as low as 0.003 $g\,cm^{-3}$), and low thermal conductivity (down to 0.017 $W\,m^{-1}\,K^{-1}$).[3] Table (2.1) sum-

Table 2.1: Property values for silica aerogels.

Property	Value range
Surface area (m^2/g)	500 - 1200[3]
Porosity (%)	80 - 99[3]
Bulk density (g/cm^3)	0.003 - 0.5[3]
Thermal cond. (W/mK)	0.017 - 0.021[3]
Dielectric const.	1 - 2[42]
Refractive index	1.007 - 1.24[3]
Sound velocity (m/s)	100[43]

marizes some property values for silica aerogels. The properties are due to the fact that air takes up most of the space inside the porous structure of the aerogels. Typically between 90-99% of the structure of an aerogel is air by volume.[34] Another important aspect of silica aerogel is its inertness and non-toxicity,[35] which contributes to making it a good catalyst support material.

Due to the interesting properties, silica aerogels have emerged as promising materials in a variety of applications. Among these are insulation,[36,37] chemical sorbents and filters,[38,39] Cherenkov radiation detectors,[40] dielectric materials,[41] as well as catalysts and catalyst carriers.[7,21]

In catalysis, many different aerogels have surfaced as suitable candidates for a variety of environmental cleaning applications, both in air and aqueous media.[7] This is especially because of their large surface area and high dispersion possibilities. Aerogels consisting of carbon, metal oxides, and mixed oxides combined with or without noble metals have been proposed as catalysts for the removal of volatile organic compounds, removal of NO_x and reforming of methane into

syngas.[44–46] The same are also eyed for support for heterogeneous catalysts in water, for example in ozonation and Fenton processes.[47,48] Some aerogels, particularly titania aerogels, posses good photocatalytic properties, which can also be improved further by doping or mixing with other elements. This enables photocatalytic degradation of pollutants as another option.[7] Aerogels are, however, still not commercially available due to expensive processing, but new advancements in the synthesis can potentially change this.

2.2 Synthesis of Aerogels

Aerogels are synthesized using *sol-gel processing*, which is a wet chemical method for the synthesis of colloidal dispersions.[4,5] In particular, this an extensively used method for oxides. The process can be used to fabricate a wide variety of advanced materials in various forms, such as powders, fibers, coatings, thin films, monoliths or porous membranes. With the sol-gel method, synthesized products achieve a high purity and molecular homogeneity. Another advantage of the sol-gel process is the low processing temperature.[5]

As for synthesis of silica aerogel, the sol is a colloidal solution containing dissolved silica nuclei. There are several ways to prepare this solution, and one of the most widely used precursors have been using a silicon alkoxide, tetraethyl orthosilicate (TEOS, $Si(O_2C_2H_5)_4$). Another option is by using waterglass, an aqueous solution of various sodium silicates, as a precursor.[34] While alkoxides tend to be more expensive, waterglass has the advantage of being a cheap alternative. Waterglass also shows a higher reactivity, and results in gels with smaller pores.[49] Reacting the slightly basic waterglass with an acid will result in a solution of silicic acid, with the functional silanol

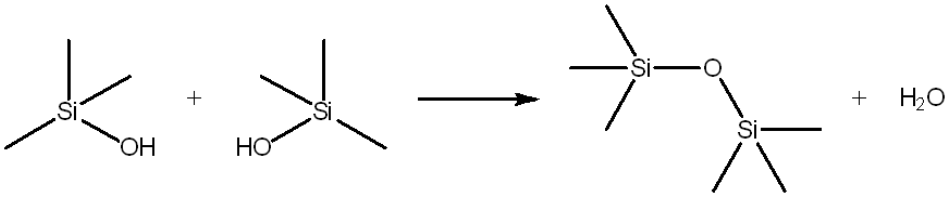

Figure 2.2: Illustration of the condensation reaction between two silanol groups, which takes place in the sol.

group (Si−OH) ready for further reactions. For the case of silicic acid, the monomer, or building block, can be represented as $Si(OH)_4$.

Upon gelation, the sol loses its fluidity and becomes a solid. For silicon alkoxides, this usually happens over a series of condensation (Eqs. 2.1-2.2) and hydrolysis (Eq. 2.3) reactions.[4] For silicic acid however, there is no need for a hydrolysis reaction because there are no ether groups, and only condensation reactions will occur, following Equation (2.1). Whichever precursor is used, in the making of silica aerogel, what happens during condensation is the silanol groups condense to form siloxane bridges (Si−O−Si).[50] This is illustrated in Figure (2.2).

$$(OR)_3Si{-}OH + HO{-}Si(OR)_3 \xrightarrow[-H_2O]{} (OR)_3Si{-}O{-}Si(OR)_3 \quad (2.1)$$

$$(OR)_3Si{-}OH + RO{-}Si(OR)_3 \xrightarrow[-ROH]{} (OR)_3Si{-}O{-}Si(OR)_3 \quad (2.2)$$

$$(OR)_3Si{-}OR + H_2O \xrightarrow[-ROH]{} (OR)_3Si{-}OH \quad (2.3)$$

Both condensation and hydrolysis are multi-step processes that occur sequentially and in parallel. Additionally, condensation of the monomers can be catalyzed by an acid or base. After the monomers self-condense into dimers and trimers, these continue to bond together

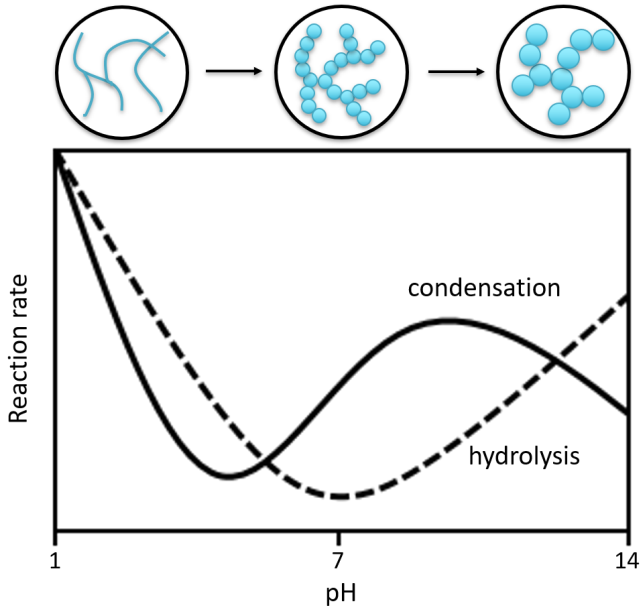

Figure 2.3: The pH dependence on the relative rates of the hydrolysis and condensation reactions, as well as their effect on the gel network. Adapted with permission from Dorchec et al.[43] Copyright 2008 Elsevier.

and form silica primary particles, which in turn combine and form larger secondary particles. This is an example of non-linear polycondensation, and is a process which keeps going until all of the sol has become an interlinked network.

2.2.1 Effect of pH

As mentioned, the gelation process can be catalyzed by the use of acids or bases. This is done by promoting the condensation and hydrolysis

reactions that are taking place, both of which are occurring via bimolecular nucleophilic displacement reactions.[51] The final structure is dependent on the pH during gelation, as is illustrated in Figure (2.3).

Under acidic conditions, the condensation reaction rate becomes slower on larger silica particles. Reactions at terminal silicon atoms are favored for electronic reasons, which promotes the development of more linear chains of particles. As the network is made up by condensation of small clusters, this growth model has been called reaction limited cluster (-cluster) aggregation (RLCA).[3]

Under basic conditions, on the other hand, the condensation reaction is promoted for larger particles. Because of the increasing acidity of the silanol proton, reactions are instead favored at silicon atoms which already have many cross-links. This promotes the development of more bulky chains of molecules, resembling a string of pearls. Since the clusters grow mainly by condensation of monomers, this model has been called reaction limited monomer-cluster growth (RLMC).[3]

While basic conditions give larger particles and larger pores, acidic conditions give smaller pores and more polymer-like molecules. This poses another challenge for acid catalyzed gels upon drying, as the smaller pores makes diffusion of the pore liquid harder.[52]

2.2.2 Effect of Aging

When the sol first transitions into a gel, the solid network is weak, as the number and strength of the links between the particles are small. This is because only a fraction of the solid particle clusters actually contribute to the continuous network at the gel point, something which might be deceiving as per the name. The composition of the gel at the

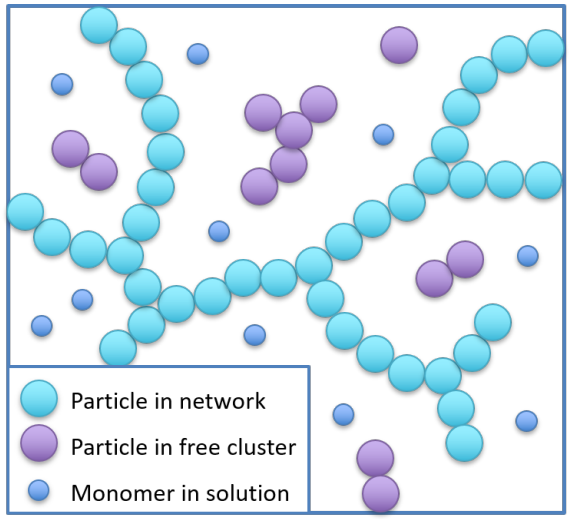

Figure 2.4: Composition of the gel at the gel point, the transition between sol and gel. Adapted with permission from Bisson et al.[50] Copyright 2003 Taylor & Francis.

gel point is illustrated in Figure (2.4). It is important to acknowledge that chemical reactions are still transpiring at this point.[3] The pore liquid in the gel is essentially a sol containing uncondensed monomers and clusters which slowly condense to the formed network. Moreover, the gel network is still flexible, allowing neighboring silanol groups to approach each other and react into siloxane bridges.[3] Aging is the process of giving the gel additional time to solidify, thus gaining a more complete and strengthened gel network.

An additional mechanism that occurs during aging is a coarsening effect akin to Ostwald ripening, caused by different solubility at curved interfaces.[53,54] Because the hydrolysis and condensation reactions are reversible, dissolution will take place in thermodynamically unfavor-

able places, followed by condensation in a more favorable place. Such places are small pores, crevices and interparticle necks.[3] The Ostwald ripening effect is driven by a reduction in surface free energy through a decrease in total surface area. This process results in thicker interparticle necks, as well as softened particle surfaces. The pore size distribution will also shift towards larger values, as more pores will become larger and smaller pores will grow shut.[53]

By introducing an aging step in the synthesis, the solid network can be reinforced by the formation of additional siloxane bridges.[3,50] Lastly, aging can be accelerated by temperature, pH, water content, or addition of some more precursor solution. Too aggressive conditions can however result in complete dissolution or destruction of the structure.[55]

2.2.3 Drying

Because the gas component is what differentiates aerogels from classical wet gels, the most crucial step in aerogel synthesis is the substitution of the liquid component with the gas. The challenge with drying the gel lies with the large capillary forces and the high surface tension at the liquid-vapor interface. This results in compression which cause the fragile gel structure to shrink and collapse upon drying under normal circumstances.[55] Instead of an aerogel, this results in what is known as a *xerogel*, which is only microporous and has significantly less surface area due to the collapsed structure.[34] To circumvent the effect of the capillary forces, a number of variant methods have been developed, such as supercritical drying, freeze drying, and ambient pressure drying.[50]

Supercritical drying (SCD) was the first method developed, and was the method used by Kistler in 1931 when he first prepared aerogels.[2] This method involves high pressure and heating of the gel above the supercritical point, where the phase boundaries between liquid and gas disappear. Here the liquid becomes a supercritical fluid, a substance that possesses properties of both a liquid and a gas at the same time. In this way, the liquid component can be removed from the gel without causing collapse.

Freeze drying avoids the capillary forces and the tension involved by freezing the wet gel, and then having the "pore liquid" sublime under vacuum to obtain an aerogel, or what is then called a *cryogel*.[3] A new problem that arises with this method however, is that crystallization of the pore liquid may distort or directly damage the gel network, unless the pore liquid has a low expansion coefficient.[56]

The *ambient pressure drying* (APD) method however, utilizes surface modification to change the properties of the aerogel before drying it at more practical conditions.[6] In this way, the pore liquid can be exchanged for a liquid with less surface tension, which then prevents the collapse of the gel network upon evaporation. Compared with SCD, this method is less expensive and the dangers associated with high temperatures and high pressures are avoided.[6]

2.2.4 Surface Modification

Surface modification, as used for APD, can be performed on the gel in order to reduce shrinkage and collapse while drying. This is done by the addition of chemicals which react with the surface of the gel, acting as surface modifying agents, in addition to an organic solvent to

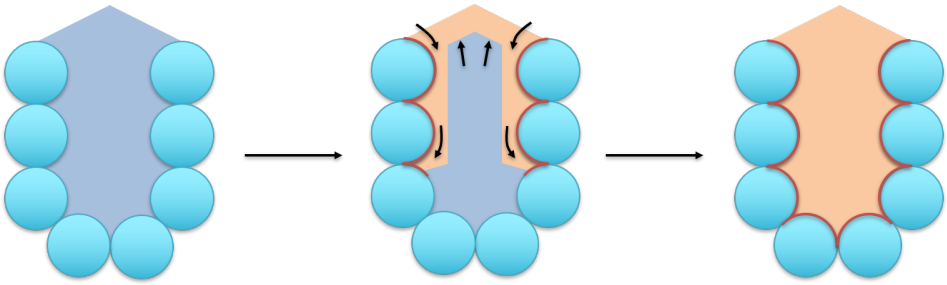

Figure 2.5: Illustration of surface modification and simultaneous solvent exchange happening in a pore.

replace the pore water.[34] Examples of such chemicals are hexamethyldisilizane (HMDS) and hexamethyldisiloxane (HMDSO). They react with the hydrophilic silanol groups on the particle surfaces and turn them into hydrophobic trimethylsilyl (TMS) groups.[57] Because of the silylation reactions, they are also known as silylation agents. Equation (2.4) shows the silylation reaction with HMDSO, and Equation (2.5) shows the reaction with HMDS.

$$2\,(\equiv\mathrm{Si{-}OH}) + \mathrm{Me_3Si{-}O{-}SiMe_3} \xrightarrow[\mathrm{H_2O}]{} 2\,(\equiv\mathrm{Si{-}O{-}SiMe_3}) \qquad (2.4)$$

$$2\,(\equiv\mathrm{Si{-}OH}) + \mathrm{Me_3Si{-}NH{-}SiMe_3} \xrightarrow[\mathrm{NH_3}]{} 2\,(\equiv\mathrm{Si{-}O{-}SiMe_3}) \qquad (2.5)$$

Water is formed as a by-product during the reaction with HMDSO. For the analogous silylation reaction with HMDS however, ammonia is formed.[57] This is important to consider, as it acts as a base catalyst and pushes the solution pH into the range where the condensation rate is higher, leading to rapid gelation.[43] HMDS is also known to react with other available hydroxyl groups (−OH), including water or alcohol, also in these cases producing ammonia as a by-product.[57] As

the modification takes place, more and more of the organic solvent will replace the water in the pores. This is illustrated in Figure (2.5). In the end, the water will exist as a separate phase below the organic phase, and the solvent exchange will be completed.

2.2.5 Methods of Synthesis

In the *surface derivatization* (SD) method, the surface modification of the gel is done after gelation and before the drying.[34,58] For this step, the gel is immersed in a solution of the silylation agents and an organic solvent, e.g. HMDS and n-heptane respectively. The silylation agents then modify the gel from the outside and inward, and the organic solvent replaces the water in the pores in a process which may take several days. Because silylation agents such as HMDS also react with the water in the gel pores, a large amount is needed in order to compensate.[43] The surface modification step can also be repeated. Following this step, the surface modified gel is washed to remove excess chemicals.

The *co-percursor* (CP) method takes a different approach to the surface modification step. In this method, the silylation agents are added to the sol near the gel point, but before gelation has occurred.[34] It should be noted that the silylation agents in this manner also can be used as catalysts for the gelation, remembering that HMDS forms ammonia which leads to increased pH. After addition, the sol should be stirred vigorously to disperse the silylation agents before gelation. The idea behind this approach is having the silylation agents well distributed throughout the pores, and thus modifying the gel from the inside. After gelation, the wet gel is then immersed in an organic solvent for simultaneous silylation and solvent exchange.

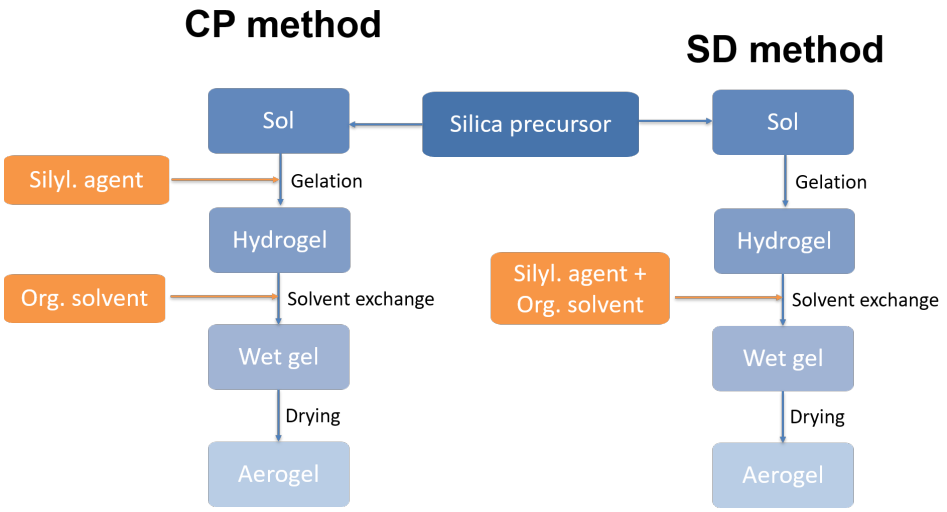

Figure 2.6: Comparative illustration of the CP and the SD methods.

Comparatively, the CP method has been found to be much faster and more economic than the SD method. This is because of the lengthy solvent exchange and washing steps that are necessary in the SD approach, as well as the considerable less amount of surface modifying agents used in the CP approach.[43] A study by Rao et al. also found that gels made from the CP method were more efficiently modified and showed a higher degree of hydrophobicity.[59] A combination of the CP method in combination with APD was developed by Bhagat et al. in 2007.[60] With waterglass as the silica precursor, this provided a simple, rapid and cost-effective synthesis route for aerogel powder.

2.3 Aerogel as a Catalyst Carrier

First of all it should be mentioned that silica is one of the most popular supports in heterogeneous catalysis. What then makes silica aerogel attractive as a catalyst carrier is the interconnected (both micro- and meso-) pore system, the large surface area, the non-toxicity and the chemical inertness.[7,8,35] The efficiency of a catalyst is dependant on the dispersion of the active phase throughout the support. The reason why surface area is so important is because the catalytic reactions happen on the surface, and the catalytically active phase are therefore the surface atoms of the catalytic phase.[61] Thus, a larger surface area leads to higher dispersion of the active phase. The porous network of aerogels are of importance because it governs the reactant and product selectivity of the catalyst.[61] Moreover, the highly versatile sol-gel process which is used for preparation of aerogels is certainly useful for tailoring the properties of the material for specific needs, and is also useful for obtaining a uniform distribution of the active phase.[7,8] In addition to this, catalyst carriers should also be mechanically and thermally stable, which are important factors for implementation of the material.[61]

There are a lot of reports regarding additions to the aerogel structure by the means of introducing various transition metal ions (TMI), such as copper,[20,62] cobalt,[22,63,64] vanadium,[62] rhenium,[23,63], molybdenum,[23] titanium[65] and iron.[24,25,27] Most of them use expensive precursors and the SCD method, but more recently APD has also been applied. By the author's knowledge, incorporation of TMI has generally been done in three different ways; the first being by making a mixed oxide gel, the second being by introducing TMI clusters or nanoparticles into the pores of the gel, and the third being by incorporating isolated TMI into the gel framework as single-sites.

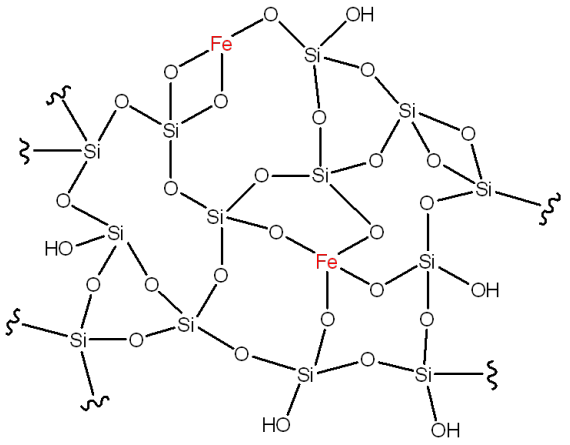

Figure 2.7: Silica aerogel structure with single-site iron incorporated.

2.3.1 Single-Site Catalysts

The term *single-site* has to do with the conformation of the active site of a catalyst. An active site of a catalyst refers to the specific location on the catalyst compound where the reaction takes place. With this in mind, single-sites can be characterized by spatially separated and isolated active sites all having identical local chemical surroundings.[18] This is to help insure the active sites are readily accessible and have an equal energy of interaction with the incoming reactants. A cation in single-site should not have any oxo bridges (M – O – M) connecting it to other cations of the same element.

Originally, the term comes from homogeneous catalysts, in which evenly distributed active sites with identical chemical surroundings can be found. The downside of homogeneous catalysis however, is the separation, recovery and recycling of the catalysts. Single-site hetero-

geneous catalysts (SSHC) on the other hand, is a newer concept which has gained increasing interest in later decades.[18] The concept is similar to homogeneous catalysts, only the single-sites are incorporated into solid materials instead, thus countering the main disadvantage of separation for homogeneous catalysts.

With a modified aerogel as a SSHC, the aerogel is the catalyst carrier (or support) while the introduced species act as the active sites for a given reaction or reactions. In this work, iron is the wanted guest element which is to be incorporated into single-sites. The coordination of such sites are most likely tetrahedral, like silicon, or octahedral. Distortion of the site geometry is also not unlikely due to the amorphous silica matrix. It is also possible that surface sites are only 3-coordinated, as was reported by Tuel et al.[26] A proposed structure of an aerogel SSHC is illustrated in Figure (2.7), in which iron is occupying a tetrahedral single-site in the framework and is 3-coordinated in a surface site.

In 2011, Kristiansen et al.[20] were the first to successfully synthesize an aerogel SSHC containing copper (1.8-10.9 wt%), made using the inexpensive waterglass precursor and the APD method. With X-ray absorption spectroscopy (XAS), they found the single-site copper to be divalent and in octahedral coordination with siloxy groups as ligands. Kristiansen studied this new material extensively in her work,[19] focusing on optimizing synthesis parameters and catalytic performance. High catalytic activity for this SSHC was reported for the SCR of NO_x, reaching up to 67% at 450 °C.[21]

2.3.2 Metal Incorporation

TMI can be introduced to the aerogel synthesis in the sol-gel stage or in post modification via various deposition methods. An example of deposition is impregnation, which seeks to introduce TMI by grafting them to the surface of the already prepared gel matrix. On the contrary, the sol-gel method opens for an easy incorporation of the metal ion as it can be added to the sol before gelation has occurred. Sol-gel introduction is advantageous because it includes the control of homogeneity on a molecular level, which can ensure a high degree of dispersion of the introduced metal.[5] A good dispersion will result in metal sites both within and on the surface of the silica matrix, wherein the surface sites are the most important since they are the ones which are available for reactants.

With the introduction of TMI into the gel network, attention has also been given to what impact the metal has on the final structure. This is specifically with porosity in mind. Previous studies have demonstrated that several TMI in lesser amounts can lead to increases in pore widths, porosity and surface area compared to plain gel analogues. Zhu et al.[65] reported on increased pore widths and lower surface area in titanium containing gels. For the single-site copper supported aerogels, Kristiansen et al.[20] reported that changes in the microstructure led to increase in average pore size, pore volume and surface area. The pore width increased from 31-33 Å for the plain gels to 47-51 Å with increasing metal content. For the gel with highest loading (10.9 wt% Cu) however, the detected surface area was roughly half of the plain gel. Håbrekke had similar observations on cobalt supported aerogels.[22]

Specifically regarding iron, Kristoffersen reported larger pore widths and pore volume, but lower surface area for his iron containing gels compared to plain gels.[24] Higher iron content resulted in a decrease

in porosity. Similarly, for iron-silicon mixed oxide aerogels, Fabrizioli et al.[25] reported decreasing pore volume and surface area for increasing amounts of iron, but also an increased average pore size for low amounts.

The presence of TMI in the sol have also been reported to act as a catalyst for gelation and have a similar effect as to base catalysts.[66] In accordance with this, observations of shorter gelation time for increasing metal content have been reported, both for Cu^{2+}, Co^{2+} and Fe^{3+}.[20,22,24,27] Additionally, it has been reported that the larger particles resulting from base catalysis appear more capable of incorporating guest cations.[20,67]

Because metal speciation matters, an inert atmosphere appears to be favorable during introduction of TMI to prevent the formation of oxides. Multiple sources have reported on using an inert atmosphere of nitrogen or argon during the introduction of iron into zeolites.[10,68–70] The introduction via ion exchange have been carried out with the protective atmosphere because these conditions are stated to affect the nature of the iron species and appear to be beneficial for the incorporation. Therefore, a similar approach is worth trying out for aerogel incorporation as well.

2.4 Regarding Iron

Iron is a first row transition metal with atomic number 26. It is a very abundant element on earth,[9] and has been well known to humans for ages. Iron is in group 8 of the periodic table, within the d-block, and has the electron configuration $[Ar]3d^64s^2$ in its ground state. Because of its configuration, the most stable oxidation states of iron are the

divalent ion, often called *ferrous* iron, and the trivalent iron, often called *ferric* iron.

In minerals, iron have been found to inhabit both tetrahedral and octahedral sites. Ferrous iron is most likely to occupy octahedral sites, whereas ferric iron is most likely to occupy tetrahedral ones.[71] The mineral colors of iron are earthy and include the colors yellow, orange, red, brown and black. For example, hematite (α-Fe_2O_3) appears reddish brown to black, magnetite (Fe_3O_4) appears black, wüstite (FeO) appears grey with a green tint, maghemite (γ-Fe_2O_3) appears brown to bluish black, and goethite (FeO(OH)) appears yellow to brown and black.[72]

As the most common ions are the di- and trivalent ions, these are the most likely for sol-gel incorporation. It can be noted however, that high-oxidation-state iron ions also exist, such as Fe(IV) in $[FeO_4]^{4-}$ and Fe(VI) in $[FeO_4]^{2-}$, but the low-oxidation-state Fe(II) and Fe(III) ions are by far the most stable.[73] In solution, iron ions are known to form complex ions together with water molecules. The typical complex ions are octahedral, with six ligands, and are called hexaaquairon complexes accordingly. Since there are two low-oxidation-state ions, there are also two variants of the hexaaqua complex for iron, namely the ferrous hexaaqua complex ($[Fe^{II}(H_2O)_6]^{2+}$) and the ferric hexaaqua complex ($[Fe^{III}(H_2O)_6]^{3+}$). Because water is a low-field ligand, both are high-spin complexes.[73]

Both complex ions are acidic, although the ferric hexaaqua complex is more acidic than its ferrous sibling due to the larger charge on the central atom and thus the stronger pull upon the electrons from the ligands. This results in the ferric hexaaqua complex easily being hydrolyzed to the ferric pentaaquahydroxo complex ($[Fe(H_2O)_5(OH)]^{2+}$), following the reaction in Equation (2.6).

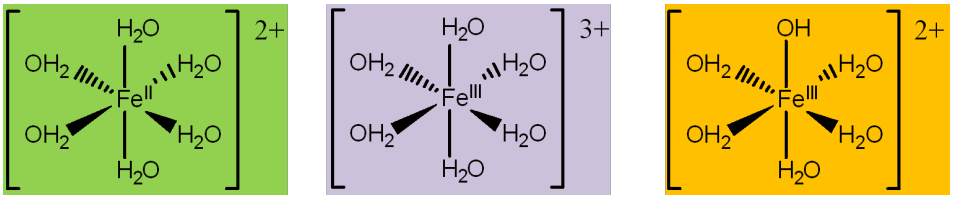

Figure 2.8: From left to right, the structures and colors of the ferrous hexaaqua, ferric hexaaqua and ferric pentaaquahydroxo complexes.

$$[Fe(H_2O)_6]^{3+} + H_2O \rightleftharpoons [Fe(H_2O)_5(OH)]^{2+} + H_3O^+ \tag{2.6}$$

The hydrolyzed complex is more often the main species in an aqueous solution containing ferric ions. Further proton loss can also continue at higher pH, ending with a neutral complex which precipitates. While ferric complexes can be oxidizing, ferrous complexes are reducing, thus Fe(II) is often oxidized by air to give Fe(III) instead.[73] This is also the case in solutions of aqueous media.

The ferrous hexaaqua complex has a pale green color in solution. The ferric hexaaqua complex, on the contrary, has a pale violet color, and the hydrolyzed pentaaquahydroxo complex has an orange color, illustrated in Figure (2.8). The color of the latter complex is the one normally observed for aqueous solutions of ferric ions due to the strong color, varying from yellow in dilute solutions through orange and to brown in concentrated solutions.

In aqueous solutions containing chloride anions, e.g. made from ferric chloride, there has been some discussion regarding which ions are forming.[74–76] The inclusion of chloride-containing complexes such as the octahedral pentaaquachloro and trans-chloro complexes, as well as the tetrahedral tetrachloro complex, have made it challenging to

find the prevailing species.

Moreover, in aqueous solutions containing silicic acid, studies have shown that ferric ions can also form relatively stable complexes with polymeric silica.[77,78] For this case, deprotonated silanol groups can act as mono- or bidentate ligands in the complex formation as presented in Equation (2.7). This complex formation between ferric ions and silica is of particular interest as it appears highly advantageous for the incorporation of iron into the aerogel network.

$$\mathrm{Si(OH)_4 + Fe^{3+} \rightleftharpoons Si(OH)_3OFe^{2+} + H^+} \tag{2.7}$$

2.4.1 Iron in Catalysis

Iron has found use as a catalyst in a number of reactions, counting among them the well known Haber-Bosch process for ammonia production and the Fischer-Tropsch process for the making of hydrocarbons.[79,80] In these processes, various iron particles are used. The Haber-Bosch process uses a promoted iron oxide with metal surface, whereas in the Fischer-Tropsch process a promoted iron carbide iron oxide species is used.

For the sake of this thesis, an important field of interest for iron is the conversion of methane into more useful chemical products. In the enzyme methane monooxygenase (MMO), which catalyze the conversion of methane to methanol, a di-iron species acts as the active site.[11] With the help of large proteins, reactions at this dimetallic site lead to the activation of O_2 and the relatively inert C–H bond found in methane and other alkanes, making MMO unique because it is the only catalysts known to be able to hydroxylate methane at ambient

temperatures. Inspired by this enzyme, researchers worldwide have tried to replicate this reaction in new catalysts for decades.[12–17,81]

Many are based on porous materials like zeolites, and especially ZSM-5 has gained attention for its high catalytic activity towards the conversion of methane. Studies on ZSM-5 containing between 0.5-6 wt% Fe show conversion of methane to phenol with high selectivity and yield.[14–16,82] The inorganic matrix is thought to provide improved stability of the isolated TMI redox site similar to as the protein mantle protects the active site in MMO. It is also evident that heat treatment causes migration of the tetrahedral framework sites into extra-framework sites, and both have been suggested as active sites in iron containing ZSM-5. In the work of Otsuka et al.,[17] tetrahedral single-site iron was suggested as the active site in a $FePO_4$ catalyst, with the Fe(III)/Fe(II) redox pair playing a crucial role in the partial oxidation of methane. An iron carbide species has also been suggested as the active site for conversion of methane to aromatic hydrocarbons.[82]

Silica has also been used for support for iron catalysts. Nozaki et al.[83] grafted iron onto SBA-15 silica and reported high selectivity for oxidation of benzene. Moreover, they reported little to no change in the tetrahedral coordination of iron after heat treatment at 300 °C, in contrast to the previously mentioned zeolite catalysts. In 2014, Guo et al.[12] reported on excellent catalytic activity for SiO_2 with 0.5 wt% Fe in single-site for the direct non-oxidative conversion of methane to ethylene. With a low iron loading, as well as low surface area ($<1\,m^2\,g^{-1}$), this efficiency was attributed to the single-site conformation which is suggested to catalyze formation of methyl radicals. The single-site also appears to hinder C−C coupling and thus the unwanted coke deposition which eventually clogs the pores.[84]

With this in mind, one can see the potential of using iron in future catalysts. With several different approaches, much depends on the nature of the active iron site as well as the carrier material. Combining the documented performance of the single-site conformation with aerogel as a promising catalyst carrier material, a new and efficient heterogeneous catalyst for methane conversion could very well see the light of day.

2.5 Characterization

Many methods can be used to characterize different properties of materials. In this Section, the five characterization methods used in this work are presented and their relevance is explained for aerogel based catalysts.

2.5.1 X-Ray Diffraction

X-ray powder diffraction (XRD) is a common analytical technique which uses X-rays to analyze a material for its crystallinity. The working principle of the technique is the diffraction of monochromatic X-rays by atoms in a material.

Diffraction is a consequence of specific phase relationships established between two or more waves that have been scattered by an obstacle, such as an atomic plane. This phase relationship between the waves depends upon the path length traversed by the waves after the scattering event, and can either be constructive or destructive depending on the how much in phase the waves are. Constructive interference

occurs when the scattered waves are still in phase and reinforce each other, while destructive interference sees the waves annul each other because they are out of phase.[85]

Equation (2.8) is known as Bragg's law, and is an expression which relates the wavelength of the X-ray and the interplanar distance to the diffraction angle. If this condition is satisfied, constructive interference is generated.[85]

$$n\lambda = 2d\sin\theta \tag{2.8}$$

Here, n is the order of reflection and is a positive integer, λ is the wavelength of the incident X-rays, d is the interplanar distance, and θ is the angle of the diffracted beam.

In a diffractometer, X-rays are generated by a cathode ray tube and are filtered to produce monochromatic radiation. Incident radiation interacts with the powdered material and produces a diffracted beam, which is then collected by a counter. By scanning the material through a range of 2θ angles, as well as rotating the sample and the counter, all diffraction directions are obtained. A recorder then outputs the signal from the counter as a diffractogram, which shows peaks of intensity where the Bragg condition has been satisfied.[85] Diffractograms are unique for every crystal system. Conventional XRD has a detection limit of 2 nm, at which point low signal to noise ratio makes small particles hard to detect.[86]

Because aerogels are meant to be amorphous, XRD can be used to exclude any crystalline phases present in the structure. While crystalline phases produce narrow peaks, amorphous phases will scatter the X-rays in many directions leading to a bump over a wide range,

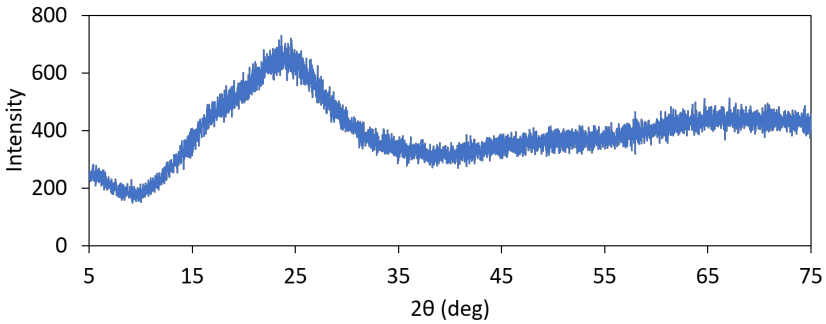

Figure 2.9: XRD diffractogram of an amorphous silica aerogel.

with less intensity.[87] The diffractogram for silica aerogel therefore does not have any sharp peaks, as can be seen in Figure (2.9), and neither should an aerogel with single-site iron, as the structure should remain amorphous. Undesirable sharp peaks in the diffractogram would indicate crystallinity in the structure, whether it being crystalline silica, iron oxide or some other unwanted impurity within the material.

2.5.2 Nitrogen Physisorption

The principle behind the two methods *BET* and *BJH* is the adsorption of a gas onto a material. A simple method to describe adsorption was presented by Langmuir in 1918.[88] The necessary assumptions for the Langmuir isotherm are monolayer coverage, a homogeneous surface with equivalent adsorption sites, that adsorption sites only hold one molecule each, that molecules adsorb into an immobile state, and that there are no interactions between adjacent adsorbed molecules.[89]

In 1985, six different types of physisorption isotherms were classified

by IUPAC,[90] which are presented in Figure (2.10). These were also expanded upon in 2015 to include two variations for both types I and IV,[91] but they are generally the same as before. The various types depend on the strength of the interactions between the adsorbate and the adsorbent, as well as the pore shape and size.[89]

Type I (sometimes referred to as the Langmuir isotherm) is often obtained from microporous solids with small external surfaces, with the limiting uptake being governed by the accessible pore volume. Type II represents the unrestricted monolayer-multilayer adsorption, and is the typical isotherm obtained for non-porous solids. Type III

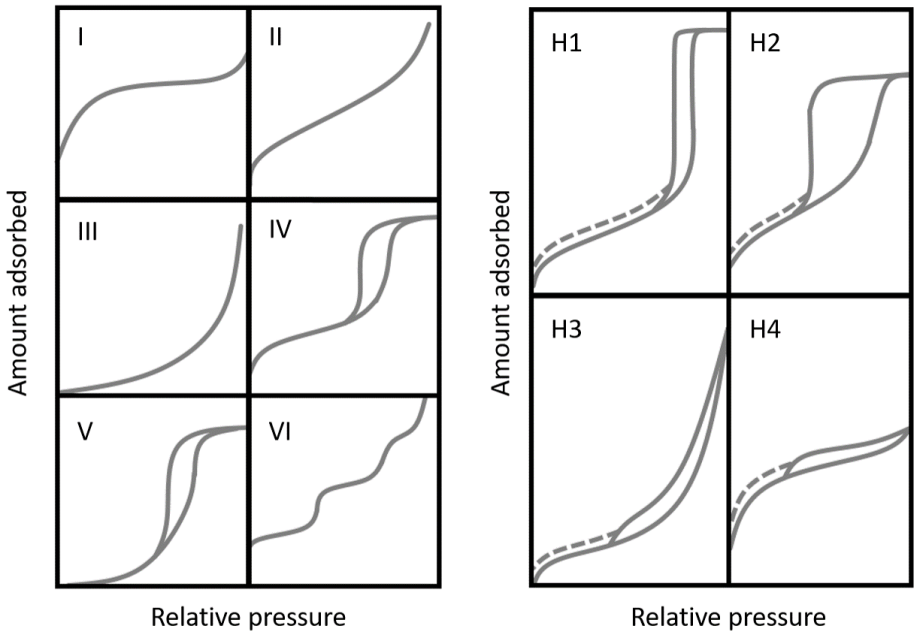

Figure 2.10: The six types of isotherms (left) and the four different hysteresis loops (right) as classified by IUPAC in 1985.[90]

is obtained when adsorbate-adsorbate interactions are strong, and is not very common. Type IV is similar to type II, shows a hysteresis loop caused by capillary condensation, and is common for mesoporous solids. Type V is related to type III, is not very common, and also shows the hysteresis loop caused by capillary condensation. Type VI represents stepwise adsorption of multilayer on a non-porous surface.[90]

In addition to the isotherm types, hysteresis loops appear when pores are present in the adsorbent material. These are caused by capillary condensation in the pores and can have varied shapes which are associated with the pore structure of the adsorbent. The four different hysteresis loops, as defined by IUPAC in 1985,[90] can be viewed in Figure (2.10). H1 is obtained from narrow and uniform pore size distributions. H2 is obtained from many porous materials where the pore size distribution is more random. H3 is obtained from materials with aggregates of plate-like particles, causing slit-shaped pores. H4 is obtained from microporous materials with slit-shaped pores. H1 and H4 can be viewed as extremes, whereas H2 and H3 are intermediates.

BET is used to determine surface area by measuring the adsorption/ desorption isotherm. The BET method is named after the men who established the theory, and is short for Brunauer-Emmet-Teller.[92] The model is an extension to the Langmuir model, applied to multilayer adsorption. Equation (2.9) shows the BET equation.

$$\frac{P}{V_{ads}(P_0 - P)} = \frac{1}{cV_m} + \frac{c-1}{cV_m} \cdot \frac{P}{P_0} \tag{2.9}$$

Here, P is the adsorption pressure, P_0 is the saturation pressure, V_{ads} is the total volume of adsorbed gas, V_m is the volume of gas corresponding to a monolayer, and c is the BET constant, which is the ratio

between the adsorption heats of the first and next molecular layer, given in Equation (2.10). The higher the value of c, the more defined is the monolayer completion point. c is considered low if < 50, signaling an overlap between mono- and multilayer adsorption. If $c < 2$, the BET method is said not to be applicable.[91]

$$C \propto \exp \frac{q_1 - q_L}{RT} \tag{2.10}$$

Nitrogen is used as probe gas for BET applications, with a working temperature of 77 K to avoid thermal motion. At a certain relative vapor pressure P/P_0, the nitrogen gas surrounds the sample material and will adsorb on both the external and internal surfaces. The amount of gas that can be adsorbed is proportional to the total surface area of the material. Assumptions for the BET method include constant adsorption energy for the monolayer and all subsequential layers of gas molecules, that layers are densely packed, that no lateral interaction occurrs between layers, and that the Langmuir model can be applied for each layer.[90] The flaws of the BET method include criticism for its unrealistic assumption of constant adsorption energy, and its usage for microporous materials which it was not developed for.[91–94] Despite this, the BET method has prevailed to this day as a universal method of determining surface area for many solids.

BJH is used to determine pore size distribution (PSD). BJH is short for Barret-Joyner-Halenda, who developed the classical pore size model in 1951.[95] The method is based on the Kelvin equation, and uses it to determine the average pore width during either adsorption or desorption of the adsorbate gas from the pores. Adsorption and desorption happen via different mechanisms in mesoporous materials. During adsorption, molecules gradually fill the pores in layers, whereas during desorption, the pores empty by withdrawing menisci. In PSD from

desorption data, a peak is often observed at approximately 38 Å due to the instability of the menisci at low pressures.[96] Simply put, the average pore size and the PSD often appear different between the two, and it has been said that adsorption depends on pore bodies and desorption depends on pore throats.[97] Similarly to BET, the BJH method also suffers when faced with small pore sizes, such as in microporous materials, because the capillary pressures can cause volumetric compressions.[98] It has been shown that BJH underestimates the pore sizes for pores below 100 Å.[96] Because of this, BJH has been called an unreliable method for evaluating pore size distributions of narrow mesopores and micropores.[91]

Aerogels have an unusual combination of small pores and high porosity which makes characterization by conventional methods such as BET and BJH difficult.[43] Nevertheless, the BET and BJH methods are useful because they provide valuable information about the surface area and the porosity, which are immensely important parameters in the case of aerogels. For silica aerogels, the surface area tend to be rather high, mostly within the range of 600-1000 $m^2\,g^{-1}$.[43] Greatly reduced surface areas might indicate a xerogel instead (when collapse has happened during drying), especially if combined with the lack of mesopores. The isotherm is usually of type IV or I, depending on the pore size distribution, with a H2 hysteresis loop. This is because of the amorphous structure of the aerogel. The hysteresis loop is caused by capillary condensation which is happening in the mesopores.[90] A random pore size distribution is expected, not a hierarchical one. Based on earlier works, an increase in surface area and porosity is expected for aerogels with TMI in single-sites.[19,20,22,24]

2.5.3 Mass Spectrometry

The principle behind *mass spectrometry* (MS) is to ionize and fragment the sample, and then separate and detect these ions to produce a mass spectrum, which is characteristic of the original compound and can be used for both qualitative and quantitative purposes.[99] Consequentially, the basic setup of a mass spectrometer consists of an ion source, a mass analyzer, and a detector, in addition to a data system which collects and processes the data from the detector.[100]

For *inductively coupled plasma mass spectrometry* (ICP-MS), the compound to be analyzed is ionized by inductively coupled plasma. This creates ions, which again fragment into smaller ions. The separation of the ions, taking place in a mass analyzer, happens according to the mass-to-charge (m/z) ratio. One of the most common mass analyzers is the quadrupole analyzer, which is a sequential filter that only allows one m/z value of ions to pass through at any given time. It is usual for the z value of the ions to be $+1$, and in that case the m/z ratio is in fact the same as the mass of the ions.[99]

When speaking of resolution in MS, it is to which degree similar masses can be identified and separated by the spectrometer, and it has been traditional to distinguish between low and high resolution. A higher resolution can be achieved by having two or more analyzers to focus and separate the ions in the same instrument, called a double-focusing spectrometer. High resolution instruments are slower and more expensive than low resolution instruments.[99]

ICP-MS can be used to do elemental analysis and determine whether and how much iron is present in the Fe-modified aerogel samples. From the principle, it is evident that ICP-MS is a destructive method, meaning the analyzed sample cannot be recovered. The amount of sample

needed, however, is in the micro- to nanogram range, so the sample consumption is of little concern. ICP-MS is also very sensitive, and it has been recommended that samples have no more than 0.2% total dissolved solids for best performance.[99] Too high amounts will give reduced detection capabilities and can cause blockage in the apparatus. Because of this, sample preparation is an important step in the analysis, and also where the most errors are caused.

2.5.4 Ultraviolet-Visible Spectroscopy

Ultraviolet-visible spectroscopy (UV-vis) is the observation of the absorption of electromagnetic radiation in the UV and visible regions of the spectrum, and is among the most widely used techniques for studying inorganic compounds.[73] The working principle of the method are the electronic transitions that occur in atoms and molecules during exposure to radiation. That is, the energy in the UV-vis range of the spectrum is used to excite electrons to higher energy levels.

There are two distinct classifications of electronic transitions, illustrated in a molecular orbital (MO) diagram in Figure (2.11). The first is d-d transitions, which are transitions of electrons between two MO which are both of metal-character (meaning the energy of the MO is closer to the metal's original orbitals than the ligands' orbitals). Secondly, there is charge transfer (CT) transitions, which are transitions between a MO of metal-character and a MO of ligand-character. This include ligand-to-metal (LMCT) and metal-to-ligand (MLCT) transitions. Absorption bands arising from CT have a much larger intensity than bands from d-d transitions because these can be forbidden by the spin and Laporte selection rules. However, d-d bands from a tetrahedral coordination are slightly more intense because they are not

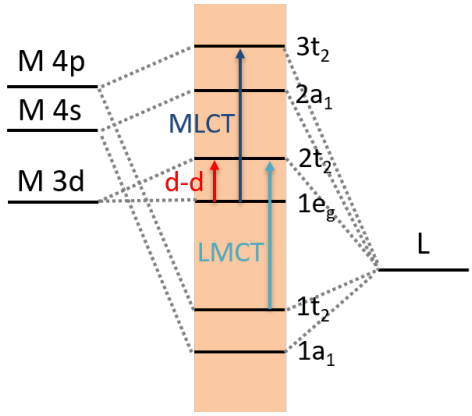

Figure 2.11: Electronic transitions in a tetrahedral complex.

Laporte forbidden.[73] The absorption wavelength at which the bands appear in a spectrum are characteristic and depends on the central metal atom, the ligands, and the energy gap between the MO.[101]

The instrument used for UV-vis spectroscopy is called a spectrophotometer. It works by producing a beam of radiation, which is usually split into two, and then measures the intensity of the sample compared to a reference. For liquid samples, the incident beam is passed through a cuvette containing the sample, while the reference is passed through an empty cuvette. For solid samples, the reflection off of the solid sample surface is more easily measured, and the reference is typically the reflection off of a white tile. In either case, a detector compares the different intensities and plots it as a function of the wavelength.

Studies of zeolites and silicates, including aerogels, containing ferric ions have found that UV-vis spectra are dominated by a large CT feature in the 200-300 nm range, in addition to weak bands extending up to about 600 nm related to forbidden d-d transitions.[10,25,26,102–104] The

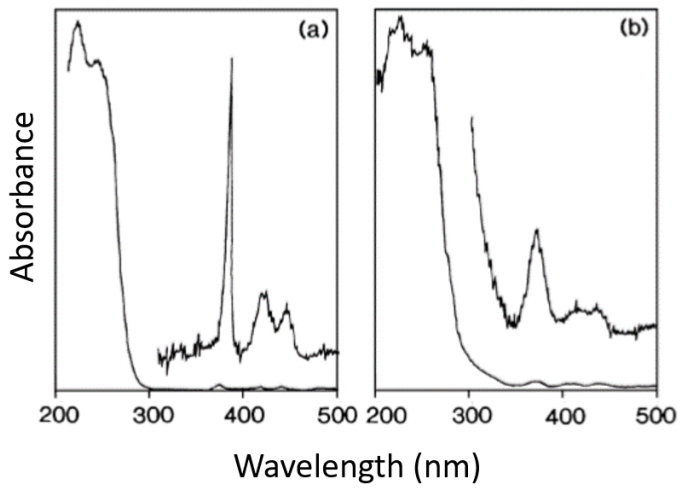

Figure 2.12: UV-vis spectra of crystalline silicalite (a) and an amorphous silicate (b) with incorporated Fe(III). The insets are magnifications of the d-d bands. Adapted with permission from Tuel et al.[26] Copyright 1998 The Royal Society of Chemistry.

strong absorption bands observed for Fe(III) are reported to be caused by LMCT transitions. Depending on the location of these bands, they have been attributed to tetrahedral and octahedral coordination of the isolated ferric ions by the simultaneous use of other charactarization methods such as EPR (electron paramagnetic resonance) and EXAFS (extended x-ray absorption fine structure). In addition, the observation of weak d-d bands located at 375, 410 and 440 nm have been considered a strong indication of tetrahedral (or distorted tetrahedral) Fe(III) in zeolite frameworks.[26]

A LMCT band at 250 nm was assigned by Fabrizioli et al.[25] to tetrahedrally coordinated Fe(III) in a composite aerogel, while bands at

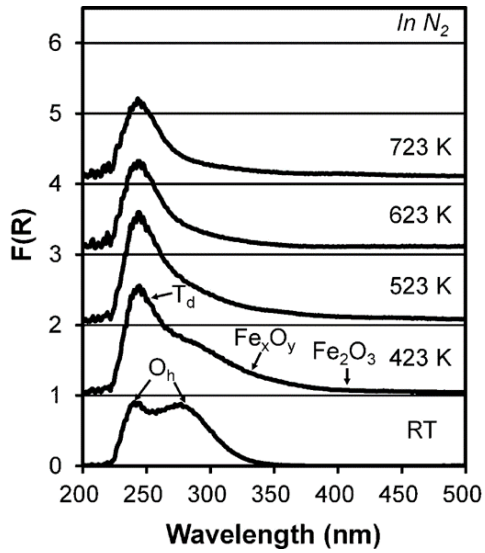

Figure 2.13: UV-vis spectra of a Fe-BEA zeolite during heating in N_2, in which the various bands assigned to Fe(III) have been pointed out. Adapted with permission from Kim et al.[102] Copyright 2013 American Chemical Society.

220 and 245 nm were similarly assigned by Tuel et al.[26] in an amorphous silicate containing iron. The UV-vis spectrum is shown in Figure (2.12). In zeolites, bands at 220, 228 and 235 nm have also been assigned to solitary tetrahedral Fe(III), whereas bands at 270, 275 and 290 nm have all been assigned to octahedral coordination.[10,102,103] Bordiga et al.[104] conducted a study on the local environments of Fe(III) in a crystalline silicalite in which they had introduced iron substitutionally using $FeCl_3$. Bands in the UV-vis spectra at 215 and 241 nm were assigned to isolated tetrahedral framework Fe(III) and later confirmed by EXAFS results. After heat treatment, a band at 278 nm was attributed to isolated octahedral Fe(III).

To summarize, it seems consistent that isolated tetrahedrally coordinated Fe(III) displays bands in the lower half range between 215-250 nm, whereas octahedral coordination appears in the higher range between 270-290 nm. This is both in crystalline and amorphous materials. Bands at higher wavelengths have been attributed to clustered iron species. According to Bordiga et al., bands between 300-400 nm come from Fe_xO_y clusters, and bands above 450 nm from larger oxide particles.[104] A broad band extending from roughly 250-700 nm is characteristic of iron oxide.[26] Figure (2.13) shows how Kim et al. assigned the bands in their Fe-exchanged zeolite accordingly.[102]

The isolated tetrahedral sites found in the composite aerogel and in the silicates do not appear that different to the characterization of single-sites introduced in Section 2.3.1.[25,26] For aerogels with single-site iron, CT bands in the 200-300 nm range is therefore expected, regardless of tetrahedral or octahedral coordination. Despite this, it should be noted that the CT bands in the spectra alone are not full proof of iron species, and are only suggestive. In addition, UV-vis spectroscopy is not quantitative, but the intensities of the bands can give an indication of the distribution of species.[10]

Chapter 3

Experimental

The powdered aerogel samples were synthesized from waterglass using the CP method in combination with APD. The same method has been applied previously in similar aerogel TMI-introduction experiments by Liu,[23] Håbrekke,[22] Kristoffersen,[24] and Kristiansen et al.[20] with varying degrees of success. An overview of the prepared samples and the synthesis parameters is shown in Figure (3.1), and in Table (A.1) in Appendix A.

3.1 Choice of Iron Precursors

The choice of iron precursors was made based on available common iron salts and on which salts have previously been used in experiments. For the similar introduction of single-site cobalt into aerogel by Håbrekke,[22] acetate ($Co(C_2H_3O_2)_2 \cdot 4\,H_2O$) and nitrate salts

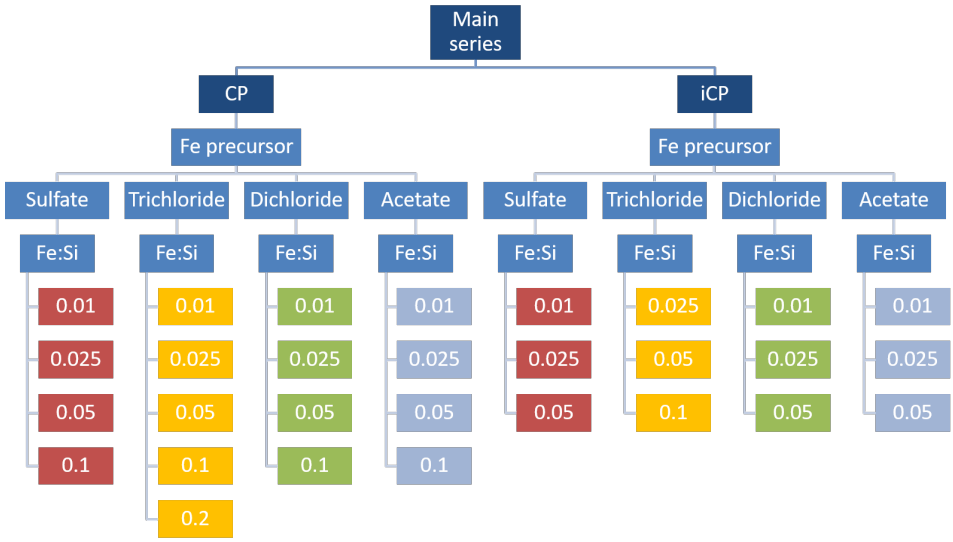

Figure 3.1: Overview of the synthesis parameters.

($Co(NO_3)_2 \cdot 6\,H_2O$) were used as the metal precursors. Kristiansen et al. also used nitrate ($Cu(NO_3)_2$) and acetate ($Cu(C_2H_3O_2)_2$) in their experiments when incorporating copper into aerogels.[20] The widely available ferrous acetate ($Fe(C_2H_3O_2)_2$) therefore seemed like a promising candidate to start with.

In the case for nitrate, incorporation of single-site iron by ferric nitrate ($Fe(NO_3)_3 \cdot 9\,H_2O$) was tested extensively by Kristoffersen,[24] yielding only a combination of iron species in line with earlier reports.[25,27] Based iron nitrate already have been tested, it was not included as a precursor for the experiments in this work.

Other common iron precursors include iron chlorides ($FeCl_2$ and $FeCl_3$), iron citrates ($FeC_6H_6O_7$ and $FeC_6H_5O_7$), iron oxides (FeO, Fe_2O_3 and Fe_3O_4), and iron sulfates ($FeSO_4$ and $Fe_2(SO_4)_3$). Among these how-

ever, the oxides are insoluble in water solution, and the citrates are only slightly soluble. Because of this, the selected iron precursors were the water-soluble iron(II) dichloride tetrahydrate ($FeCl_2 \cdot 4\,H_2O$), iron(III) trichloride hexahydrate ($FeCl_3 \cdot 6\,H_2O$), and iron(III) sulfate hydrate ($Fe_2(SO_4)_3 \cdot XH_2O$). All iron precursors were bought from Sigma Aldrich.

3.2 Preparation of Sol

To make the silicic acid solution (SA, H_4SiO_4), the initial waterglass solution (sodium silicate, Na_2SiO_3, 27 wt% SiO_2, Sigma-Aldrich) was diluted with distilled water to a solution of 8 wt% (1 M) SiO_2, and then ion exchanged using Amberlite IR120 hydrogen form (Sigma-Aldrich) in a column with a 1:1 volume proportion. It was assumed that the entire waterglass solution was ion-exchanged going through this. The slight variation in water content was a result of the ion exchange column setup. In the resulting SA solution, the pH was found to be approximately 3 by the use of pH-paper. This was to make sure the value did not become too high, which in turn would result in early gelation. The SA solution was continuously stirred using a magnetic stirrer.

3.3 Procedure for CP Method

Figure (3.2) illustrates the procedure for the CP method. The SA solution was evenly distributed into small beakers, each of which were continuously stirred using magnetic stirrers. The appropriate amount

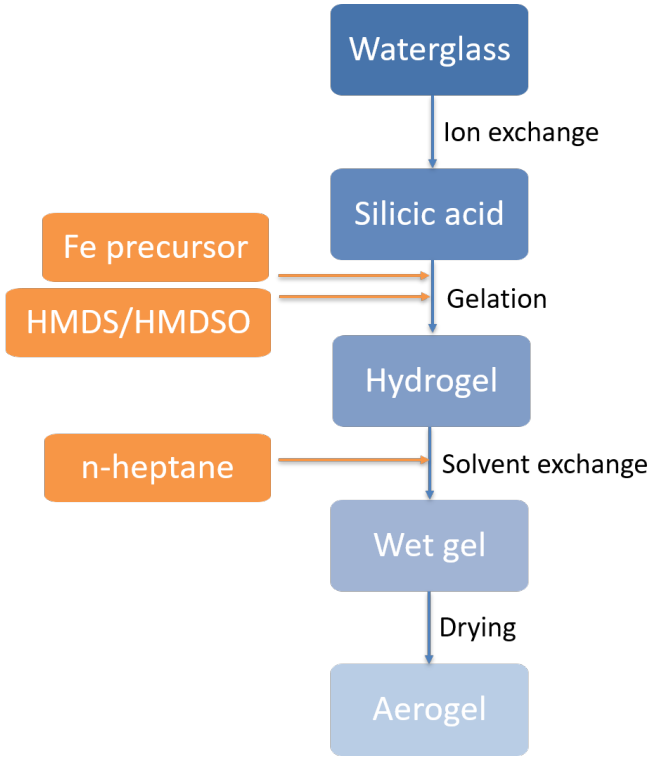

Figure 3.2: Illustration of the CP method synthesis route.

of iron precursor (Fe:Si = 0.01, 0.025, 0.05, 0.1, 0.2) was then added to the stirring SA solutions, followed by addition of silylation agents HMDS (hexamethyldisilizane, $HN(Si(CH_3)_3)_2$, Sigma-Aldrich) and HMDSO (hexamethyldisiloxane, $O(Si(CH_3)_3)_2$, Sigma-Aldrich). The ratios of the silylation agents were Si:HMDS:HMDSO = 1:1.1:1.0, which is similar to Kristiansen et al.[20] At this point, the solution was stirred vigorously to ensure thorough mixing.

After the initial gelation had occurred, the gels were left for aging for

approximately 1 day. The wet gels were then transferred over to a new beaker for the washing and pore water exchange. The washing was intended to remove loose iron species in the pores, and was done with methanol (CH_3OH, VWR Chemicals) two times before pore water exchange with n-heptane (C_7H_{16}, VWR Chemicals). The beakers were covered by aluminium foil. After approximately 1 day, the liquid phase was collected by decantation.

3.3.1 Procedure for CP with Inert Gas

The synthesis has also been carried out in a controlled nitrogen atmosphere, using the experimental setup as shown in Figure (3.3). This was with the intention to help prevent oxidation of the iron species, and was inspired by a similar approach for zeolites.[10,68,69] Figure (3.4) illustrates the procedure for the iCP method. The SA solution was kept in a closed system after the ion exchange titration, and until the gelation was completed after the addition of HMDS and HMDSO by

Figure 3.3: Experimental setup used for inert atmosphere.

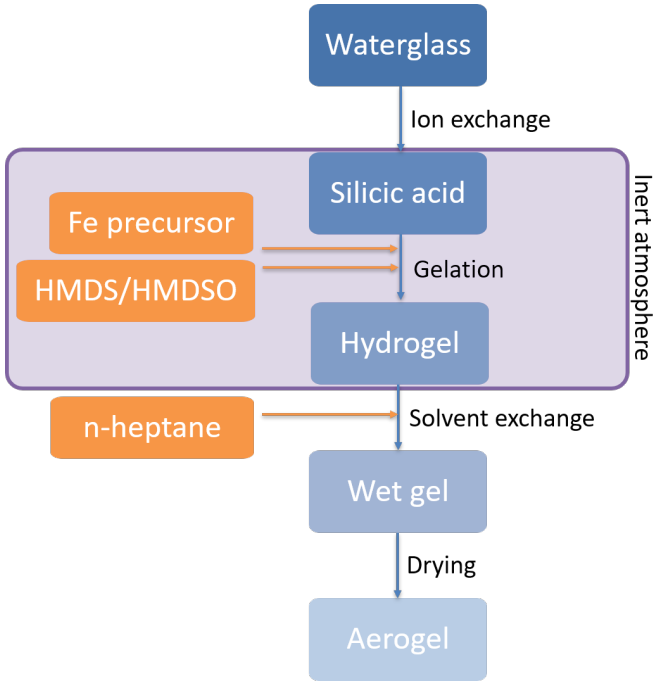

Figure 3.4: Illustration of the iCP method synthesis route.

syringe. The steady flow of nitrogen was only stopped briefly during addition of the iron precursor.

In a separate experiment, a round and a pear-shaped flask were also tested out to look for major differences between the two. In this experiment, iron dichloride (Fe:Si = 0.025) was used as the iron precursor. The round flask was stirred by a magnet, but this was not possible in the pear-shaped flask.

3.4 Drying Procedure

After the washing and pore water exchange step, the samples were transferred to Petri dishes to be dried in static air at ambient pressure in a furnace (APD). The drying procedure was as follows: 18 h at 65 °C, 3 h at 85 °C, and finally 2 h at 150 °C with a heating rate of 5 °C min^{-1}. This was the procedure used by Kristiansen et al.[20] After the drying, samples were mortared into fine powder. Samples without further heat treatment are called as-prepared.

3.5 Heat Treatment

Further heat treatment was also applied to the as-prepared samples to test the thermal stability. The heat treatment was done in static air in a furnace. Two different heating programs were used, referred to as *annealing* and *calcination*. Annealing was done at 450 °C for 30 min, with a rate of 5 °C min^{-1}. Calcination was done at 700 °C for 3 h, with a rate of 10 °C min^{-1}. All samples were subject to annealing, but only the samples with the molar ratio Fe:Si = 0.025 were subject to calcination. Samples subject to heat treatment have a tag at the end of their names to indicate which have been applied, this being *-an* for annealed samples or *-cal* for calcined samples.

3.6 Instrumental Data

3.6.1 XRD

The XRD instrument used was a Bruker D8 A25 DaVinci X-ray Diffractometer with a CuKα radiation source operating at 40 kV and 40 mA, and a LynxEye^{TM} SuperSpeed Detector. Data was collected from 5-75° 2θ over 15 min, using a constant slit opening of 6 mm and a step size of 0.013° with a counting time per step of 0.56 s.

3.6.2 BET and BJH

For BET and BJH analysis, the instrument used was a Micrometrics Tristar 3000 Surface Area and Porosity Analyser. Both adsorption and desorption curves were measured for a total of 91 points. Before the measurement, the samples were degassed using a Micrometrics VacPrep 061 Sample Degas System for removing water and other volatile adsorbents. Degassing was carried out at 250 °C under vacuum for approximately 1 day.

3.6.3 ICP-MS

The instrument used was an Element 2 HR-ICP-MS from Thermo Electronics, and the analyses were carried out by Syverin Lierhagen. Before introduction, the samples had to be decomposed. 20-40 mg of the samples were weighed out and digested by addition of concentrated hydrofluoric acid (HF, 0.1 g) and concentrated nitric acid

(HNO_3, 1.5 mL). The samples were then transferred to a large Teflon flask and diluted with MQ-water to a weight of 216.6 g to ensure preservation of the samples in HF (0.23%) and HNO_3 (0.1 M). Teflon tubes (16 mL) were then filled with the sample solution ready for analysis. Three blank samples were also prepared to eliminate background noise.

The weight fraction of an element in a sample was calculated using Equation (3.1).

$$wt\% = \left(\mathrm{x}\frac{\mu g}{g} \cdot 10^{-6} \frac{g}{\mu g} \right) \cdot 100\% \tag{3.1}$$

3.6.4 UV-Vis Spectroscopy

UV-vis spectra were measured using a Hamamatsu High Power UV-vis Fiber Light Source equipped with an integrating sphere and an *i*-trometer detector from BWTEK. The samples were measured over the range of 200-1000 nm, using an integration time of 2000 ms and an integration multiplier of 4. A dark scan and a reference scan of a perfectly reflecting material were conducted before each measurement.

The UV-vis spectra are presented here using reflectance instead of absorbance, since these appear less noisy and were therefore easier to work with. The noise was due to the experimental setup used and the detector. Therefore, the bands appear as valleys instead of peaks, but this does not affect the location of the bands as the horizontal axis is the same.

3.7 Naming of the Samples

The samples have been named according to the scheme described as follows. Firstly, the synthesis method is denoted by *CP* for co-precursor method (in air) or *iCP* for co-precursor method with inert atmosphere. Then, the molar ratio of iron (Fe:Si) is denoted by a number, followed by (II) or (III) denoting either Fe(II) or Fe(III) in the precursor. After this is a tag denoting which iron precursor was used: *-Ac* for iron acetate, *-Cl* for iron chloride, or *-Sulf* for iron sulfate. Lastly, samples which have received additional heat treatment after synthesis are denoted with *-an* or *-cal* for samples annealed at 450 °C or calcined at 700 °C, respectively. Samples without any of these are as-prepared samples without further heat treatment.

Two samples do not follow this scheme however, as the important parameter for this particular series was the flask shape. These samples are instead tagged with *-pear* or *-round* referring to a pear-shaped or a round flask, respectively.

As an example, take the sample *iCP-0.05(III)-Cl*. This has been made via the CP method using the inert atmosphere. The molar ratio Fe:Si = 0.05, with the iron in the precursor being Fe(III). Finally, the precursor used was a chloride, specifically ferric trichloride. Because there are no more strings to the name, this sample is as-prepared, and has not received any further heat treatment. The sample *iCP-0.05(III)-Cl-an* is the same sample, only after it has been annealed at 450 °C.

Chapter 4

Results

The synthesis has been carried out using the CP method, with and without inert atmosphere, and the parameters which have been varied were the iron precursor and the amount of iron. Two different flask shapes for the inert gas experiments were also tested out. The samples have been characterized by XRD, BET, BJH, ICP-MS and UV-vis spectroscopy, as well as by observations of color, gelation time and hydrophobicity.

4.1 Observations

Simple observations were done during and after all the various syntheses. These include color observations of the solutions, gels and powders, as well as gelation time and hydrophobicity. These observations are subjective, as they were not carried out by instruments.

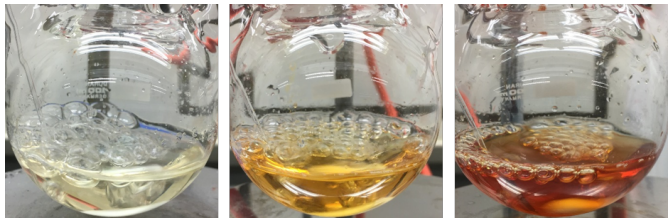

Figure 4.1: The orange appearance of the sol after addition of iron.

Observations were made of the color from the sol stage and through drying. Both for the sulfate, trichloride and acetate series, the sols appeared pale yellow to orange depending on the amount of iron precursor added, shown in Figure (4.1). Only the sols from the dichloride series appeared green in color, but turned brownish during gelation. These colors match the yellow color of the ferric complexes and the pale green color of the ferrous complexes, respectively. (Figure (2.8).) The brown color appearing during gelation for the dichloride series likely signifies oxidation of the ferrous iron species.

It should be noted that the samples made with the ferrous acetate precursor did not appear green at all. This provoked a simple iron valency test of the precursor, which indicated that only Fe(III) ions were present, meaning the precursor must have been already oxidized. Nevertheless, the two acetate sample series were not re-done with a fresh precursor due to time restraints. It also appears needless to do so, seeing as the iron appears to oxidize during the sol-gel transition in any case, based on the color change observed during gelation for the dichloride series. Besides, it is possible that the oxidized acetate precursor can also be a good iron precursor.

Regardless of iron precursor, all final gel powders ended up in a shade of white to brown. Similar colors have also been reported for iron con-

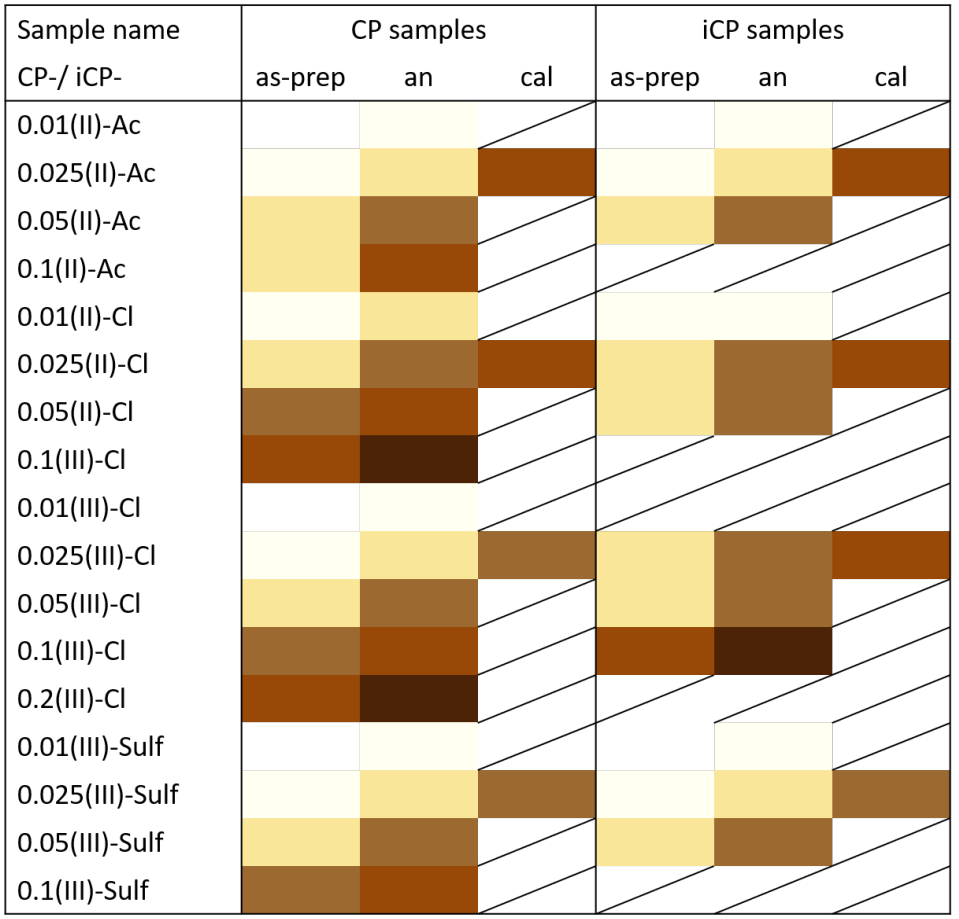

Figure 4.2: Observed colors of the dried samples.

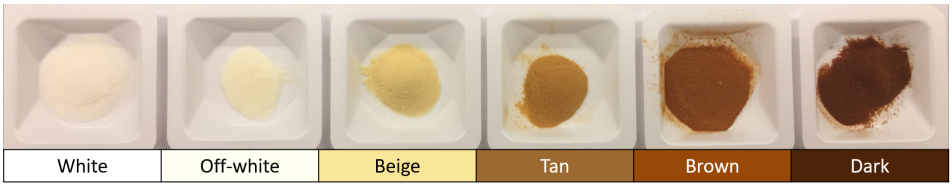

Figure 4.3: The various shades of brown displayed by the samples.

taining aerogels before.[24,25,27] The observed colors of the dried samples have been included in Figure (4.2). Organized from lightest to darkest, these have been labelled as: white, off-white, beige, tan, brown and dark. Figure (4.3) shows how these colors compare with the powder samples.

The whitest samples are the samples with the least amount of iron in them (Fe:Si $\leq$ 0.025). The color always darkens with increasing iron content, as well as with annealing and calcination. Comparing with the Fe-modified silicas by Tuel et al.,[26] they appeared white for up to 5.70 wt% Fe, attributed to iron incorporation in the framework. After a solvent extraction treatment and calcination in air at 500 °C they changed to off-white, or tan to dark brown without the additional treatment. After calcination at 600 °C, Fabrizioli et al.[25] reported on tan colors, while López et al.[27] reported different shades of orange to brown. All reports were in agreement with attributing the darkening color to the increasing presence of iron oxide particles, which is an appropriate assumption for this work as well. This means that the best candidates for single-site iron are the samples which are white or off-white in color, as the silicate samples by Tuel et al. were.[26] In particular, this includes the samples with Fe:Si = 0.025 or less.

Based on the light color and the iron content, calcination at 700 °C was only applied to the samples with the molar ratio Fe:Si = 0.025 to

Figure 4.4: Pictures showing a successful (left) and a failed (right) hydrophobicity test.

look at the changes this high temperature heat treatment would bring about. Calcination of the darker colored samples seemed redundant.

The gelation time was observed to vary between half a minute to over 3 minutes depending on the iron content. Although the exact gelation times might be somewhat subjective due to different observations of the gel point, they were decreasing with increasing iron content. This was expected due to previous observations of iron acting as a catalyst for the gelation process.[24,27,66] After gelation, extracted pore water was measured to pH=11.

The samples were tested for their hydrophobicity by adding a drop of water to the powder, and observing whether the water spread or was suspended as a drop on top of the powder remains. This is shown in Figure (4.4). All as-prepared samples held the water drop suspended, thus were found to be hydrophobic by this method. After annealing, the samples appeared to lose this hydrophobicity, as the added water drop would spread out. This was found by Kristiansen et al.[20] to be caused by the loss of the hydrophobic TMS groups, which occurred via oxidation into other species that were detected by MS. These were detected in the 250-600 °C temperature range, and happened at lower

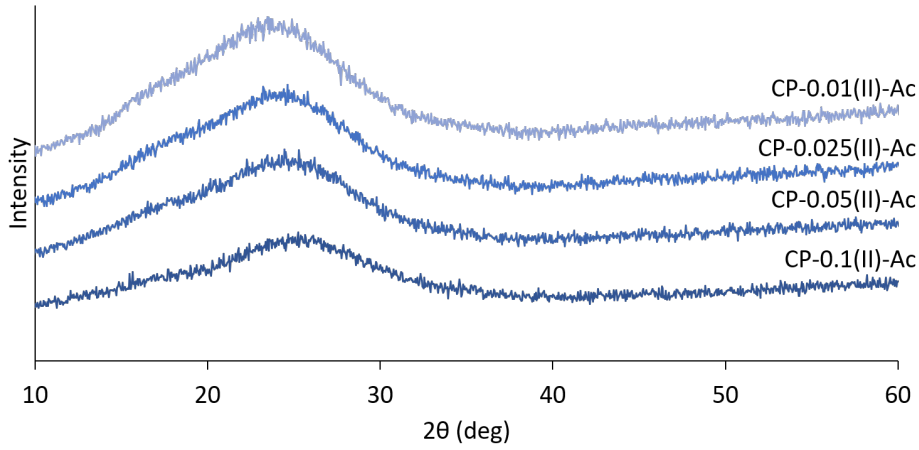

Figure 4.5: XRD diffractograms for the CP acetate series.

temperatures for the Cu-modified gels than for the unmodified gels. There is little reason for this not to be the case in Fe-modified gels as well.

4.2 XRD Results

XRD was conducted on all samples to exclude any unwanted crystalline phases or impurities in the gel structure. The XRD diffractogram for the plain aerogel sample, displayed in Figure (2.9), shows only the broad peak attributed to amorphous silica. The absence of sharp peaks in the diffractogram excludes crystalline phases within the gel. This confirmed the plain aerogel had the characteristic amorphous structure of aerogels, which is also the structure wanted for the aerogels containing iron in single-site.

Table 4.1: Overview of the XRD results.

Sample name	CP samples Amorphous			iCP samples Amorphous		
CP-/ iCP-	as-prep	an	cal	as-prep	an	cal
0.01(II)-Ac	yes	yes	-	yes	yes	-
0.025(II)-Ac	yes	yes	yes	yes	yes	yes
0.05(II)-Ac	yes	yes	-	yes	yes	-
0.1(II)-Ac	yes	yes	-	-	-	-
0.01(II)-Cl	yes	yes	-	yes	yes	-
0.025(II)-Cl	yes	yes	yes	yes	yes	yes
0.05(II)-Cl	yes	yes	-	yes	yes	-
0.1(II)-Cl	yes	yes	-	-	-	-
0.01(III)-Cl	yes	yes	-	-	-	-
0.025(III)-Cl	yes	yes	yes	yes	yes	yes
0.05(III)-Cl	yes	yes	-	yes	yes	-
0.1(III)-Cl	yes	yes	-	yes	yes	-
0.2(III)-Cl	yes	yes	-	-	-	-
0.01(III)-Sulf	yes	yes	-	yes	yes	-
0.025(III)-Sulf	yes	yes	yes	yes	yes	yes
0.05(III)-Sulf	no	yes	-	no	yes	-
0.1(III)-Sulf	no	yes	-	-	-	-

To represent the Fe-modified gels, the XRD diffractograms for the CP acetate series are displayed in Figure (4.5), while an overview is shown in Table (4.1). The smooth curves akin to the plain gel show the amorphous nature of this series and the lack of crystalline phases in the gels. This indicate that the iron containing gels retain the expected amorphous structure of aerogels despite the introduction of iron to the synthesis, and is a positive sign with regards to single-site incorporation of the TMI. The rest of the Fe-modified aerogels also dis-

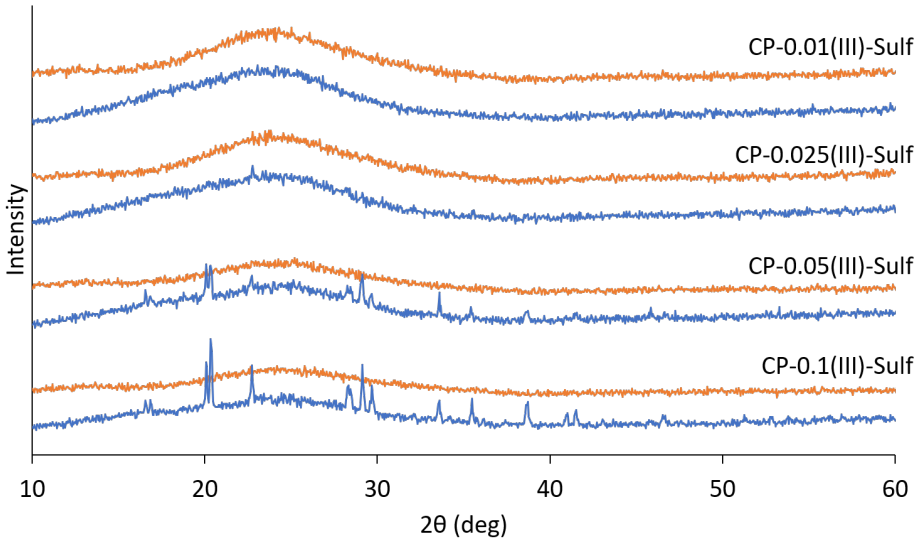

Figure 4.6: XRD diffractograms for the CP sulfate series. Blue is as-prepared and orange is annealed.

play similar smooth diffractograms. It can be noted that higher iron content flattens the curve by decreasing the intensity of the bump centered at 25° which is caused by the amorphous pure silica matrix. This suggests that increasing the iron concentration makes the structure less like the pure silica network. This can possibly be caused by a large amount of iron incorporated or deposited on the silica network, or a formation of amorphous iron oxide instead of silica. Nevertheless, the amount of iron used in this work do not appear to cause any long range crystalline phases detectable by this method.

Three exceptions to the amorphous diffractograms stand out however. In Figure (4.6), peaks indicating crystalline phases can be seen to appear in the diffractograms corresponding to gels with larger amount

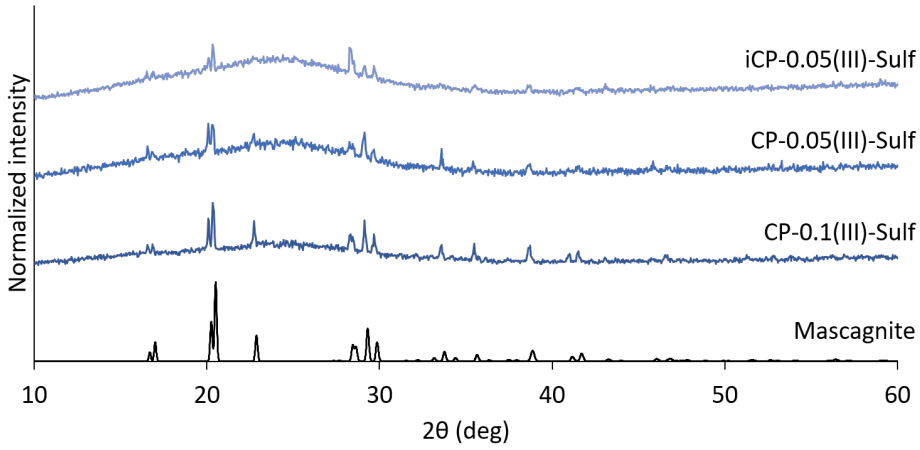

Figure 4.7: Normalized diffractograms of the gels showing crystallinity, compared to the diffractogram of mascagnite.

of ferric sulfate (Fe:Si $\geq$ 0.05). The same is also the case for the equivalent sample made with inert atmosphere, *iCP-0.05(III)-Sulf*. In Figure (4.7), these peaks are seen to correspond with the mineral mascagnite, a rare ammonium sulfate with the chemical formula $(NH_4)_2SO_4$.[72] This has most likely formed from a side reaction between the sulfate precursor and the ammonium formed by HMDS (following the surface modifying reaction, Eq. (2.5)). Further evidence was provided from the presence of small white crystals in the relevant dried samples, as seen in Figure (4.8). These crystals match the description of mascagnite as colorless, white, grey or yellow crystals which are also water soluble.[72] Because of this, it is possible the aerogel itself was actually amorphous, but contained heterogeneous crystalline impurities which were hard to separate out. Because the peaks in the diffractograms disappear upon annealing, as seen in Figure (4.6), the sulfate samples were subject to further analysis.

Figure 4.8: Small crystals were observed in *CP-0.1(III)-Sulf*.

Heat treatments of the remainder of the samples cause little to no change in the diffractograms, as no sharp peaks appear in any. All samples therefore can be assumed to remain amorphous after annealing at 450 °C, as well as after calcination at 700 °C. This is interesting because amorphous iron oxide clusters are only metastable and are expected to crystallize at elevated temperatures.[105] Even for the gels with Fe:Si ratio of 0.1 and 0.2, no notable sharp peaks arise in the diffractograms. This also surprised Kristoffersen,[24] who suggested an explanation in the form of shrinking particles. It is a likely option that small oxide particles do disperse in the pores, but rather than larger particles shrinking, it can be that iron species on the silica surface detach and form the oxide particles during annealing. This type of migration has been suggested before, with indications of iron in octahedral coordination found by spectroscopic techniques.[26,27] Calcination of the samples with Fe:Si = 0.025 at 700 °C similarly do not result in any peaks, and therefore exclude long-range crystalline phases. On the other hand, it is possible that present oxide nanoparticles in these samples are too small to be detected by XRD, and that the samples with larger iron content would show crystalline peaks if they had been subject to calcination.

4.3 BET and BJH Results

BET and BJH were applied to all samples to get information regarding the surface area and the pores. As most of the isotherms and pore size distributions obtained are quite similar, the CP acetate series is presented as an example. Data for this series is shown in Figure (4.9), while the effect of heat treatment on *CP-0.025(III)-Ac* is shown in Figure (4.10). The rest of the samples, and the obtained values, can be found in Appendix B.2.

For the Fe-modified gels, the resulting isotherms are a mix of type I and IV as defined by IUPAC, becoming more type IV with increasing iron content in the gel. Type IV is the typical isotherm displayed by mesoporous materials due to the capillary condensation in the pores.[90] This is a common isotherm for aerogels, as they are contain mesopores. The plain gel shows an isotherm of combined type I and IV character with a hysteresis loop, inferring that the gel contains micropores and small mesopores. This is not unexpected as waterglass gels have been reported to produce aerogels with smaller pores than alkoxide precursors do.[49]

The hysteresis loops fall under the H2 or H3 type, meaning the samples have a random PSD (H2), or contain aggregates of plate-like particles with slit-shaped pores (H3),[90] or a combination of these. It is expected and desired that the aerogel powders have a random distribution of pores caused by the amorphous structure, so the H2 type is the more expected of the two.

The pore size distributions were calculated from both the adsorption and the desorption isotherms during the analyses, however only the adsorption data is presented here to avoid the artefacts present in

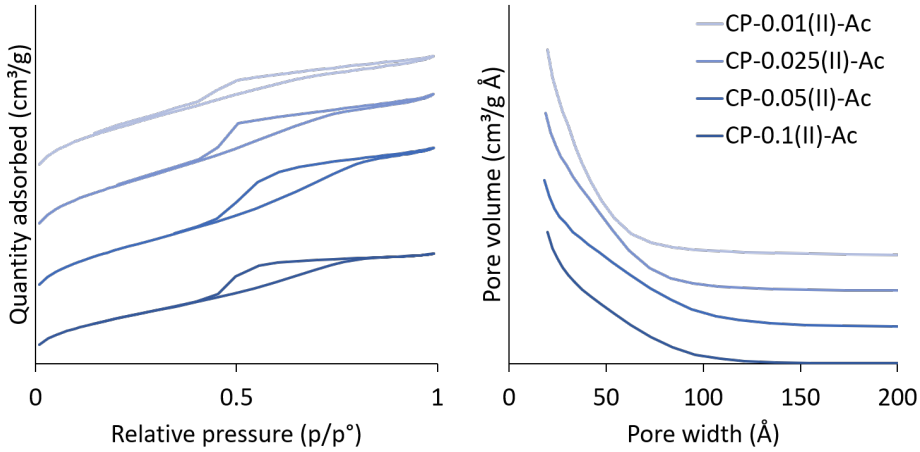

Figure 4.9: Isotherms and PSD for the CP acetate series.

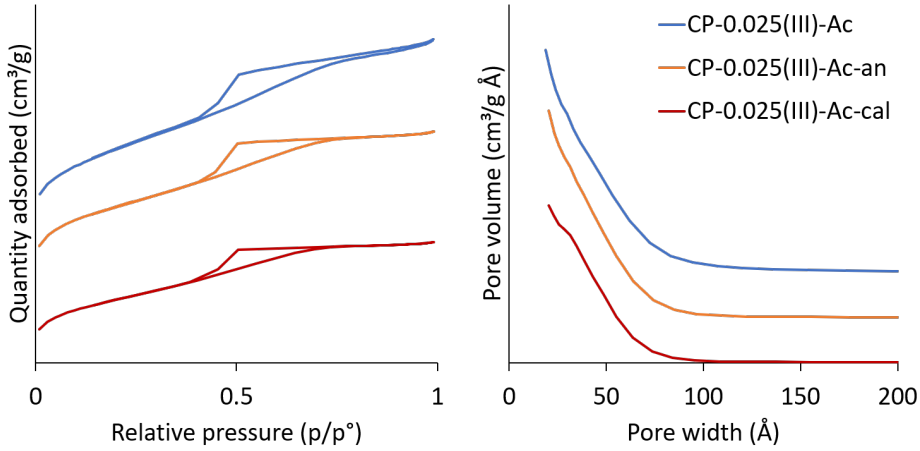

Figure 4.10: Isotherms and PSD for *CP-0.025(III)-Ac*.

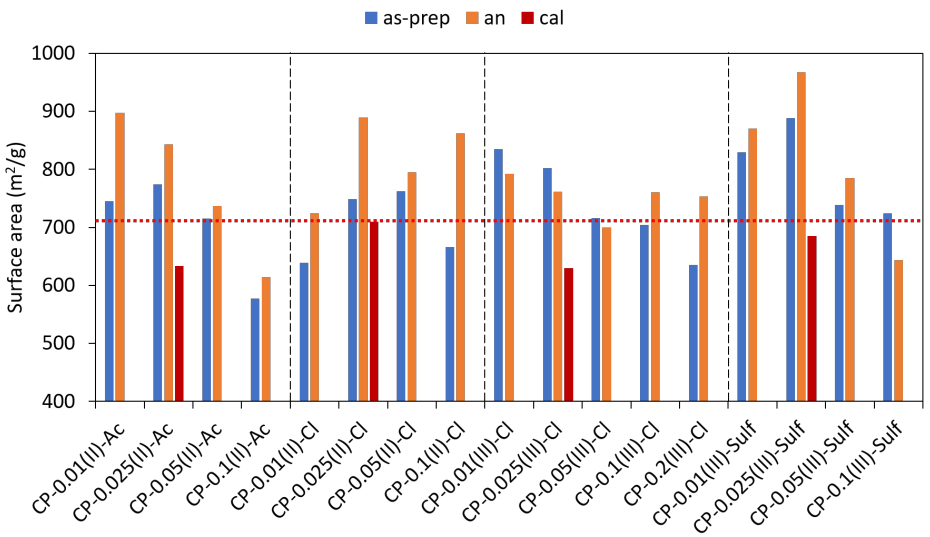

Figure 4.11: Comparison of the BET surface areas of the CP samples. The dotted line marks the surface area of the plain sample.

the PSD from desorption data. Comparatively, the data from either mostly gives the same pore volumes, but average pore widths are somewhat larger from the adsorption data. This is likely connected to adsorption data relating to pore bodies and desorption data to pore necks,[97] as was mentioned in Section 2.5.2. From the distributions it can be seen that the gels largely feature micropores and mesopores, with the average being between 35-55 Å. The random distribution can be attributed to the amorphous nature of the materials, and the size range is reasonable for the waterglass precursor and compares well with earlier reports.[20,22,24]

The surface areas for the samples, calculated using the BET method, are shown in Figures (4.11) and (4.12). The obtained values are in

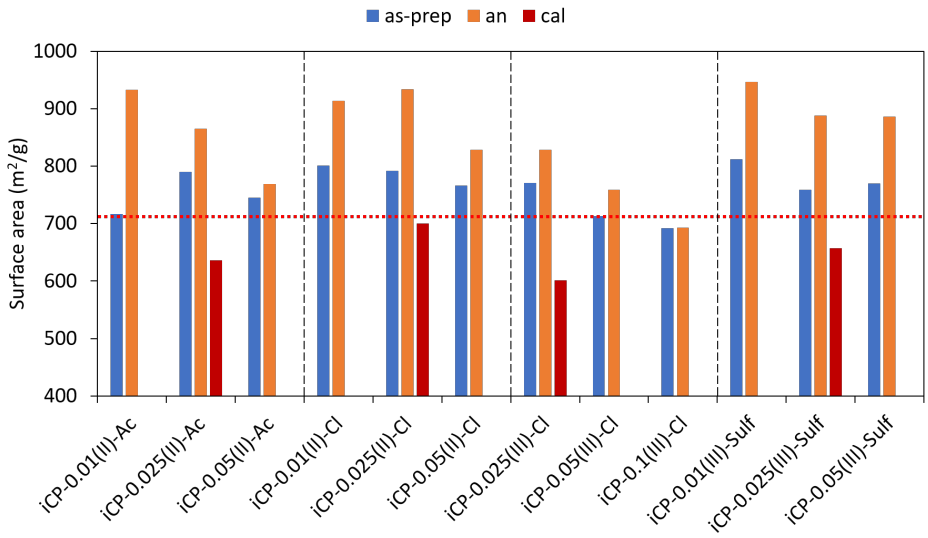

Figure 4.12: Comparison of the BET surface areas of the iCP samples. The dotted line marks the surface area of the plain sample.

the range of about 600-950 $m^2\,g^{-1}$ for all precursors and iron content variations, and fall within the reported value range in the literature as seen in Table (2.1). From the largest to the lowest values, the precursors can be ranged as sulfate > trichloride ≥ dichloride > acetate. It should be noted that the surface areas for the samples with Fe:Si molar ratio of 0.01 and 0.025 are higher (745-888 $m^2\,g^{-1}$) than that of the plain aerogel sample (714 $m^2\,g^{-1}$). A possible explanation for this increase is a stiffening or distortion of the network causing more pores. In iron oxides, the Fe−O bond distance for tetrahedral iron coordination is reported to be 1.87 Å, and even longer when in octahedral position (1.95-2.15 Å).[106] Meanwhile, Si−O bond distances vary, but 1.60 Å is an average value in many forms of silica.[107] Tuel et al. reported that the isolated iron had a distorted tetrahedral co-

ordination with two Fe−O bonds of 1.89 Å and two of 2.03 Å in their Fe-modified silicate.[26]

A similar increase in surface area was also reported for aerogels with 1.8 wt% copper,[20] but stands in contrast to previous studies for the same amount of iron.[24] Samples with higher iron content did however measure a lower surface area, and samples with Fe:Si ≥ 0.1 even measure a lower surface area (577-704 $m^2\,g^{-1}$) than the unmodified silica gel. This reduction in surface area was similarly observed for the copper gels by Kristiansen et al.[20] They attributed this reduction to shrinkage during drying and further condensation of silanol groups, caused by incomplete surface modification due to increasing amounts of surface copper species. This is because surface copper was assumed to remain hydrophilic during surface modification. It is therefore likely that surface iron species or iron oxide particles also have a similar effect.

Broader pore sizes can be seen in the Fe-modified gels compared with the average pore size of 34 Å in the plain silica gel. This is expected because it was also reported by Kristoffersen, Håbrekke and Kristiansen et al.[20,22,24] A low iron content in the samples results in larger pores and an increase in the average pore width, shown in Figures (4.13) and (4.14). This is also inferred from the type of isotherm. The larger pores can be related to iron surface species which hinder further condensation between silica particles. Largest average pore widths are obtained with a molar ratio Fe:Si = 0.05. This appears to be a threshold, as further doubling of iron content results in equal or smaller pore widths. As mentioned before, this porosity loss can be attributed to incomplete surface modification and shrinkage caused by extensive amounts of surface metal species.[20] Another possibility is the clogging of pores by iron oxide particles.

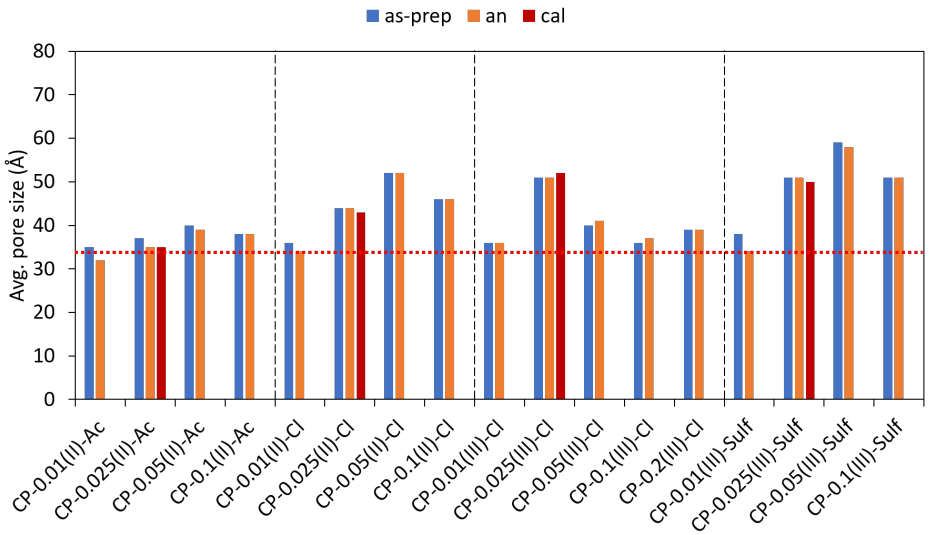

Figure 4.13: Comparison of the average pore size in the CP samples. The dotted line marks the average pore size of the plain sample.

The largest pores and pore volumes are detected for the iCP dichloride series, with average pore widths over 70 Å and pore volumes over $1.50\,\mathrm{cm^3\,g^{-1}}$. This large increase can suggest the formation of iron species on the silica surface during early gelation, which could inhibit further formation of siloxy bridges between the growing silica particles and result in larger pores. It is possible that Fe(II) was more inclined to bond with deprotonated silanol groups because of the absence of air. The dichloride precursor is further addressed later. Arranging the iron precursors after largest to smallest pores and pore volumes gives dichloride (iCP) > sulfate > dichloride (CP) > trichloride > acetate.

The general trend for heat treated samples in comparison to the as-prepared samples is an increased surface area for the gels after an-

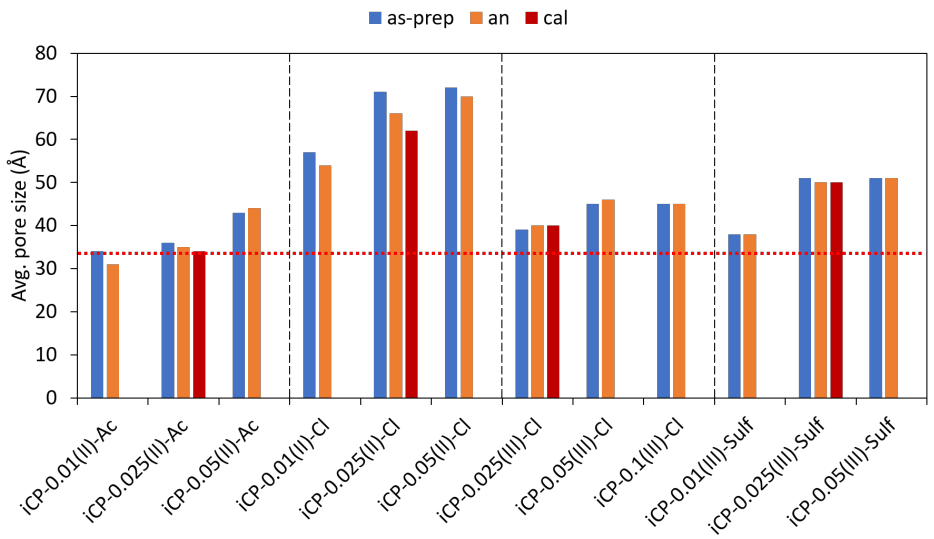

Figure 4.14: Comparison of the average pore size in the iCP samples. The dotted line marks the average pore size of the plain sample.

nealing and a decreased surface area for the gels after calcination. Only four samples deviate from this pattern by having a lower surface area for the annealed samples than for the as-prepared ones. While the PSD tend to have the same shape before and after the heat treatments, a decrease in the cumulative pore volume is detected. For instance, *CP-0.025(II)-Ac* has a cumulative pore volume of $0.83\,\mathrm{cm^3\,g^{-1}}$, which decreases to $0.66\,\mathrm{cm^3\,g^{-1}}$ after annealing and to $0.52\,\mathrm{cm^3\,g^{-1}}$ after calcination. A possible explanation for the larger surface area and lower pore volume measured is that annealing at 450 °C causes the partial collapse of some larger pores into smaller pores. Another option is that small iron oxide clusters aggregate in the pores. This would also lead to the larger surface area and lower pore volume measured, and can also be related to the darker color observed for the annealed sam-

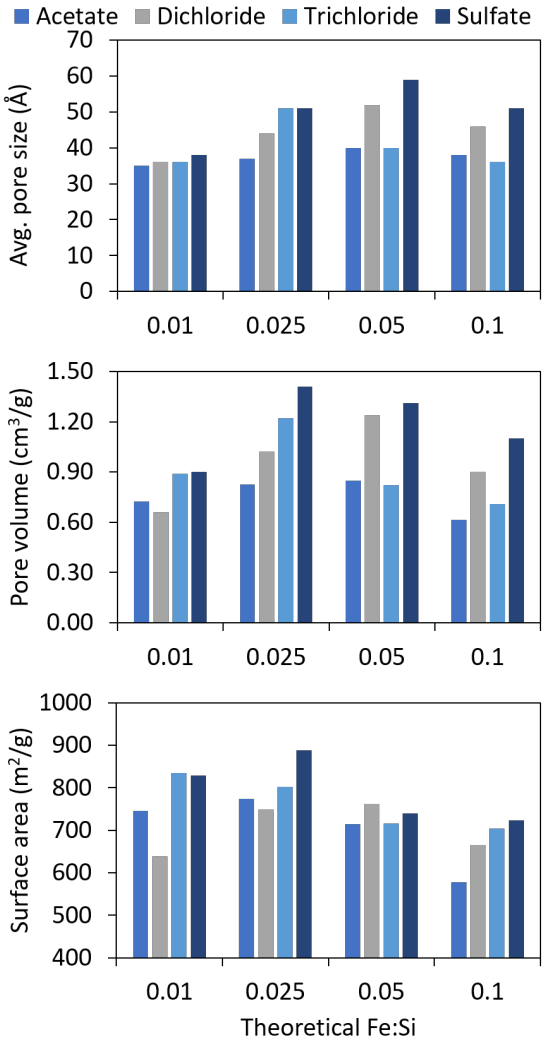

Figure 4.15: The variation of average pore size (top), cumulative pore volume (middle), and surface area (bottom) between the four iron precursors.

ples. During calcination at 700 °C it is likely that sintering occurs, compressing the gel and resulting in a lower pore volume and a surface area below the original value of the as-prepared gel. More oxide formation is also plausible at this temperature.

To summarize the influence of the iron precursors, the variations of the porosity for the CP samples are shown in Figure (4.15). While the largest average pore sizes (over 70 Å) by a fair amount are measured for the iCP dichloride series, the sulfate series generally measure larger pores overall. The sulfate samples also display the largest cumulative pore volumes, in addition to the largest surface areas. The gels made with the acetate precursor generally display the lowest values. Håbrekke observed the same between cobalt acetate and cobalt nitrate.[22]

4.4 ICP-MS Results

The two trichloride gel series were analyzed with ICP-MS to look at iron uptake in the gel with increasing amount of iron in the synthesis, and the results are presented in Figure (4.16).

The trend for iron uptake in the aerogels appears to be linear in this region, and a maximum uptake is not observed. This is contradictory to what Kristoffersen observed.[24] For his gels, there appeared to be an upper limit as samples with theoretical Fe:Si ratio of 0.17 and 0.27 both measured around 10 wt% iron. However, *CP-0.2(III)-Cl* has a calculated iron loading of 14.1 wt%, which is notably larger than both. For Kristoffersen's two samples the precursor ratios are Si:Fe:HMDS:HMDSO = 1:0.17:2.11:2.09 and Si:Fe:HMDS:HMDSO = 1:0.27:1.06:1.04, so the high silylation agent ratios in the former could

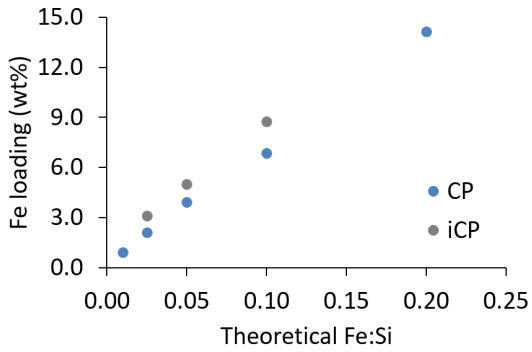

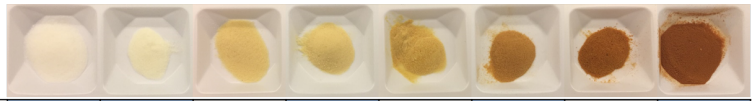

Fe loading (wt%)	0.9	2.1	3.1	3.9	5.0	6.8	8.7	14.1
Theoretical Fe:Si	0.01	0.025	0.025	0.05	0.05	0.1	0.1	0.2

Figure 4.16: The uptake of iron in the as-prepared trichloride gels, with sample colors included.

be related to the low loading. Indeed, after a parameter study by Kristiansen it was reported that excess HMDS resulted in the loss of copper in Cu-modified aerogels.[19] For the latter however, the silylation agent ratios are almost the same as the ones used for this work, and still the iron loading is lower than for *CP-0.2(III)-Cl*, despite the higher Fe:Si ratio in Kristoffersen's sample.

The color variations of the as-prepared samples with increasing iron loading are also shown in Figure (4.16), and can be seen to become darker with increasing iron content. The Fe-modified silicas by Tuel et al.[26] were white for as much as 5.7 wt% Fe, which is not the case here. As suggested earlier, the darkening color is likely an indication of iron oxides. This will be addressed again later however, as ICP-MS

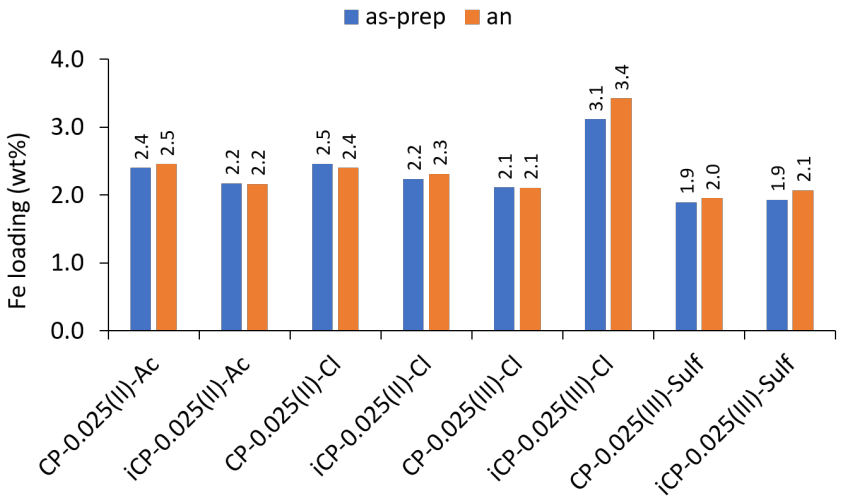

Figure 4.17: The calculated weight fraction of iron in the samples with Fe:Si = 0.025, before and after annealing.

does not provide information about iron speciation.

For all gels, the experimental Fe:Si ratio is higher than the theoretical ratio. Unfortunately, this is expected because the exact silicon content is unknown after the ion exchange procedure, as some can be trapped in the column. For the iCP trichloride series the experimental ratio is approximately double of the theoretical, but this was also the series with the largest deviation in sol volume. It is possible that too little silica was collected after ion exchange, hence too much iron was added in turn.

After analysis with UV-vis spectroscopy, the remaining samples with a theoretical molar ratio Fe:Si = 0.025 were also analyzed with ICP-MS for determination of the iron loading. These samples were chosen be-

cause of the moderate iron content and their light color, which implies a low presence of oxides and possibly iron in single-sites, as reported by Tuel et al.[26] The UV-vis spectra of these samples, which also support this, are addressed later, in Section 4.5. The calculated weight fractions of iron in these samples are shown in Figure (4.17). The experimental Fe:Si ratios have also been calculated and can be found in Table (B.2) in Appendix B.3.

The weight fractions of iron in the samples with Fe:Si = 0.025 were measured between 1.9-2.5 wt% Fe. This is except for *iCP-0.025(III)-Cl* which contained 3.1 wt% Fe, possibly due to the addition of too much iron precursor, as mentioned before. Nevertheless, the order of precursors with regards to largest uptake is trichloride (iCP) > dichloride = acetate > trichloride (CP) > sulfate. The loading of 1.9-2.5 wt% Fe is within the acceptable range found in literature for methane conversion catalysts,[14–16,81,82] albeit it could also be larger, as larger iron content is reported to relate to higher catalytic activity. Still, it should be noted that Guo et al.[12] prepared a catalyst only containing 0.5 wt% Fe, which showed great catalytic activity. The increased conversion of this catalyst was accredited to iron being in single-sites.

4.5 UV-Vis Results

UV-vis spectroscopy was applied to all as-prepared, annealed and calcined samples to get information about the iron speciation in the material, i.e. to see whether iron had been incorporated into the aerogel network as single-sites. Because the UV-vis spectra are here presented using reflectance instead of absorbance, the bands appear as valleys instead of peaks, but this does not affect the location of the bands as

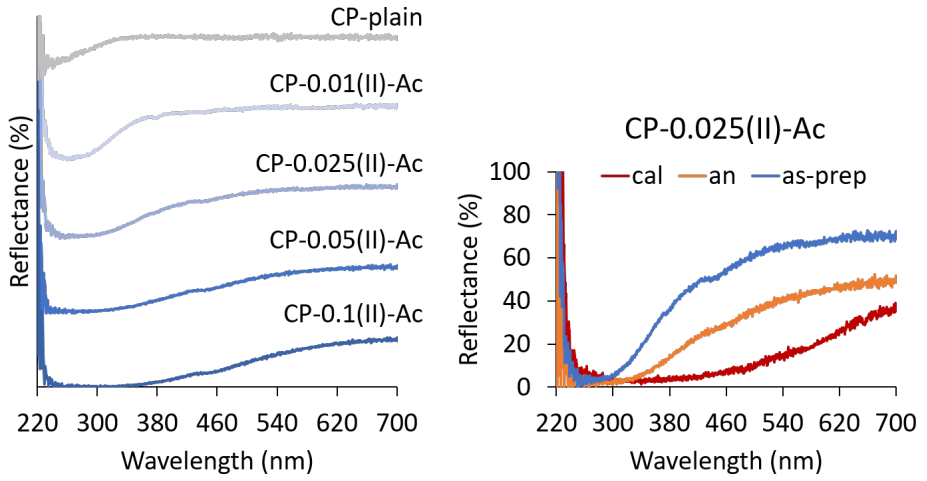

Figure 4.18: UV-vis spectra for the plain gel and CP acetate series (left), also showing the behavior of spectra from annealed and calcined samples (right).

the horizontal axis remains the same. The reason for using reflectance is explained in Section 3.6.4.

Figure (4.18) presents the spectra obtained for the CP acetate series, as well as for the plain gel. As have been reported prior for related materials containing various iron species,[10,25,26,102–104] a dominating CT feature is clearly visible in all the spectra of Fe-modified aerogel samples. Judging from the literature and comparing with the spectrum of the plain gel, the cause of the present absorption bands is attributed to the introduced iron.

The most intense band is seen to appear below 300 nm, being within the range ascribed to isolated Fe(III) sites.[10,102,103] This suggests iron has been successfully incorporated as isolated cations, potentially as

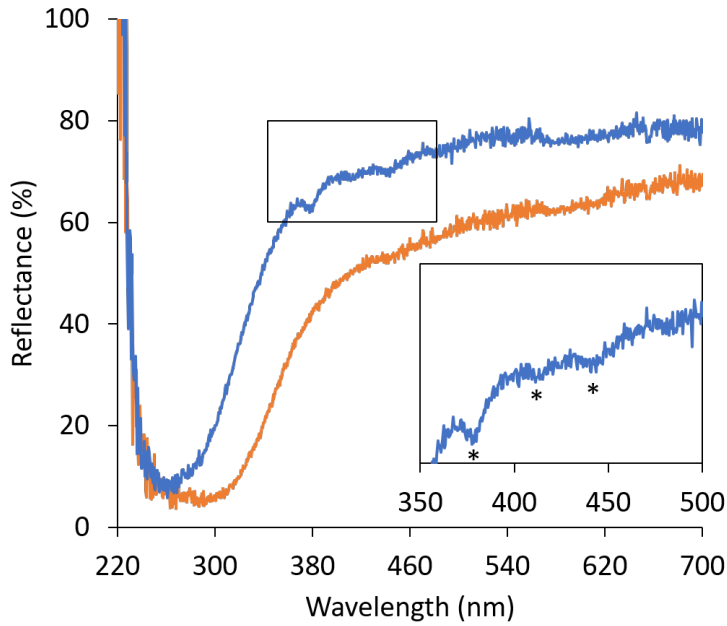

Figure 4.19: UV-vis spectra for *CP-0.01(II)-Ac* before (blue) and after annealing (orange), with an inset providing a magnified look at the region where the the possible d-d bands appear.

the wanted single-sites. It is more difficult to assign coordination, but it is not unlikely that the band located at around 250 nm can be attributed to tetrahedral sites.[25,26] The possibly broader appearance of the band is also suggested to be because of the amorphous network (Fig. (2.12)), which is naturally more flexible than the rigid structure of zeolites.[26]

Figure (4.19) shows the UV-vis spectrum for *CP-0.01(II)-Ac*. In the spectrum, there appears to be a small series of bands at approximately 375, 410 and 440 nm. Given their low intensity, these can be the d-d

bands which have previously been considered a strong indication of tetrahedral Fe(III) in zeolite frameworks.[26] This series of bands can be discerned in all samples with the molar ratio Fe:Si = 0.01, and gives further implication of tetrahedrally coordinated Fe(III) in these samples. At higher iron content, and with heat treatment, the weak d-d bands are drowned in the growing tailing feature of the more intense CT bands. Alternatively, the band at 375 nm could be a CT band suggesting the presence of oligomers, as it is located within the region that Bordiga et al.[104] assigned to such. Given the low intensity of the band however, a d-d band is more likely.

For the gels with a molar ratio of Fe:Si $\geq$ 0.025 a band is seen at approximately 450 nm. This can be attributed to larger iron oxide particles in accordance with the literature.[26,102,104] Also the darkening sample colors for samples with increasing iron content suggest this. The presence of crystalline iron oxide nanoparticles has however not been detected by XRD, but the particles might be of a size below the detection limit of 2 nm. Amorphous iron oxide particles can also be an explanation.

The bands visibly broaden with higher iron content as well as with both annealing and calcination. The trend was the same for all the precursors, and with both the CP and iCP method. This seems to give the impression that larger amounts of iron in the synthesis only cause formation of clustered iron species, such as iron oxide particles. As for the annealed samples, the band broadening contributes to the assumption that the iron ions migrate and aggregate into clusters when the samples are heat treated.[25] After calcination only a broad band is observed almost all across the 250-700 nm range, which fits well with the band described for iron oxide.[26] Nevertheless, despite the band broadening, it still retains a shoulder at approximately 250 nm, possibly inferring that the iron single-sites do not completely

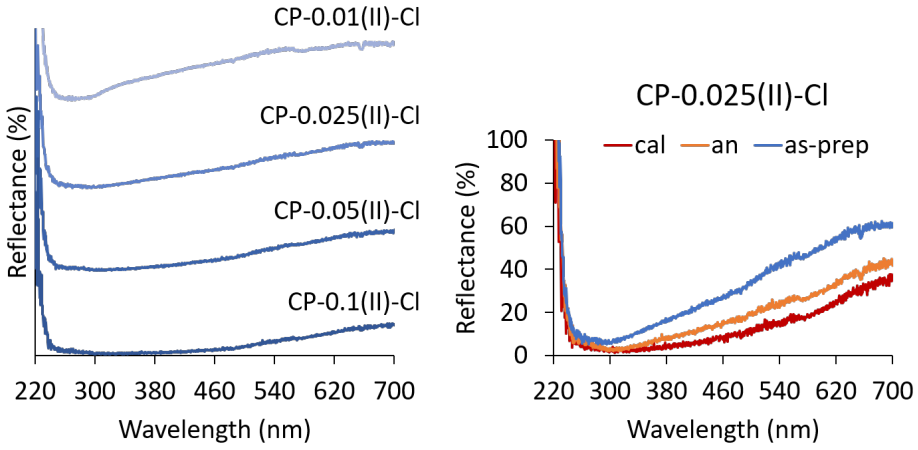

Figure 4.20: UV-vis spectra for the CP dichloride series (left), also showing the behavior of spectra from annealed and calcined samples (right).

disappear. Prior studies on related Fe-modified materials have addressed the same assumption using several spectroscopic methods including EXAFS, EPR, XPS and Mössbauer spectroscopy.[24–27] Most agree about the co-existence of several iron species in the material at higher iron loadings.

Figure (4.20) presents the spectra for the CP dichloride gels. The dichloride precursor results in more intense bands beyond the 200-300 nm range. As these bands are connected with iron oxide clusters, this suggests iron oxide nanoparticles form even for gels with a molar ratio Fe:Si = 0.01. In combination with the darker colors and the BET data, iron dichloride in particular appears to favor formation of iron oxide. This could be related to the valency, to ferrous complexes being reducing, or to the lack of stable ferrous silicate complexes, making ferrous ions less likely to incorporate into the silica matrix. It is also possible that the formation of chloro complexes such as tetrachloroiron

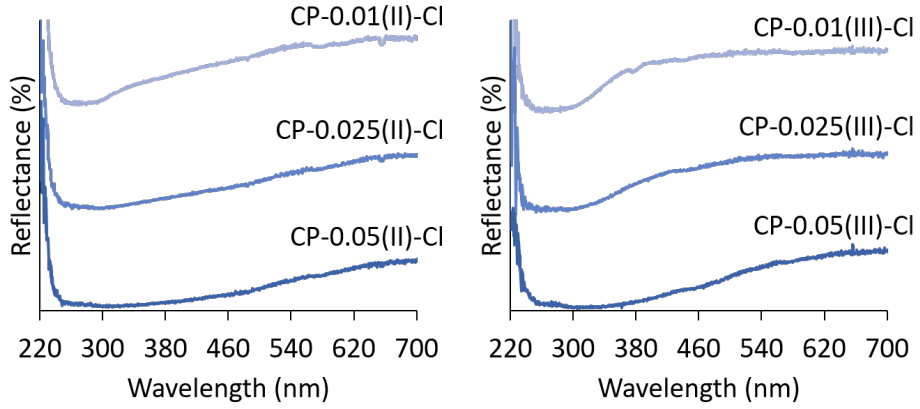

Figure 4.21: Comparison of UV-vis spectra from the CP dichloride (left) and the CP trichloride samples (right).

is what disrupted the incorporation with the silica network, and in turn promoted the formation of oxide particles during gelation. A similar effect however, does not seem to be the case in the trichloride gels. In Figure (4.21), the CP dichloride and trichloride series are compared to each other. Once more, this suggests the increased presence of clustered iron species for the gels prepared with iron dichloride. The other three precursors all appear more suitable for avoiding iron oxide formation in gels with low iron content.

In the end, only the gels with Fe:Si molar ratios of 0.01 and 0.025 are assumed to contain single-site iron as the prevailing iron species. The prepared aerogels with higher iron content potentially contain a mix of different iron species, as have been the case in previous works.[24,25,27] If the intensity is used suggestively as a rough indication of distribution, about half of the iron appears to be in single-sites at the highest iron content or after heat treatment. However, the rest of the iron has likely turned into oxide form, which is not the desired outcome.

4.6 Flask Shape

A test run of the two flask shapes was run to see if any major differences were observed between the two. The resulting gel samples are of matching beige color, and no difference in color is seen between the annealed and calcined gels either. Both gels were also found to be hydrophobic by the same method as the rest of the samples. Structurally, both samples are confirmed amorphous by XRD. With nitrogen physisorption, the isotherms of both are found to be of type IV with hysteresis loops of type H2.

The largest differences between the two gel samples are in the porosity. The sample *iCP-pear* measures larger surface area and pore volume than *iCP-round*, but equal average pore widths are measured, listed in Table (4.2). This can imply the gel surface is more effectively modified in the pear-shaped flask, which could be a result of the converging cone bottom making the bubbling of the nitrogen gas spread across all of the solution. Even so, it is hard to say how this makes a more

Table 4.2: Obtained data for the flask shape series, including BET surface area (S_{BET}), cumulative pore volume (V_p), average pore width ($\overline{D}_p$), Fe loading, and experimental Fe:Si molar ratio.

	iCP-pear		iCP-round	
	as-prep	an	as-prep	an
S_{BET} (m^2 g^{-1})	804	887	672	653
V_p (cm^3 g^{-1})	1.17	1.16	0.92	0.80
$\overline{D}_p$ (Å)	46	45	46	46
Fe loading (wt%)	1.8	-	2.1	-
Exp. Fe:Si	0.026	-	0.027	-

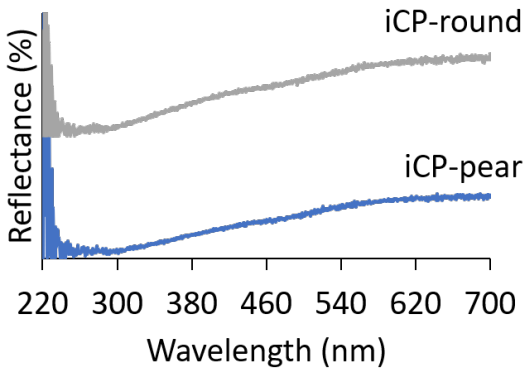

Figure 4.22: Comparison of the UV-vis spectra for the two gels made using different flasks.

homogeneous solution than the regular stirring in the round flask. In addition, a higher iron content is detected by ICP-MS for the gel made with a round flask, with the loading calculated to 2.1 wt% Fe versus 1.8 wt% Fe. This is not a large difference, however.

In Figure (4.22), the UV-vis spectra for both samples are presented. Neither stand out, as both show the same profile of broad absorption bands over a wide range, suggesting both samples contain iron oxide particles or a combination of iron species, as mentioned earlier.

Based on the data obtained here, the shape of the flask appears to affect the porosity of the aerogel as both samples were made from the same batch with otherwise equal conditions. However, judging from the similar color and the UV-vis spectra, the flask shape does not appear to make a difference regarding the incorporation of iron into the gel network as single-sites.

Chapter 5

Discussion

The most important properties which make aerogels highly attractive in catalysis are the large surface area, which is important for the dispersion of active catalyst, and the interconnected pore system, which is important for selectivity.[7] With the incorporation of a guest element such as iron into the gel structure, it is crucial that the aerogel structure is not compromised, but that it retains the signature traits of plain silica aerogel. Therefore, the following criteria for the aerogel structure are established: The Fe-modified aerogels must remain amorphous, they must be porous in the micro and meso regimes, and they must possess a large surface area. For this criterion, a surface area above the plain aerogel sample will be set as the lower limit, approximately at $700\,\mathrm{m^2\,g^{-1}}$. These criteria are to assure that the pores are interconnected and well-accessible, and that as much area as possible is available in order to increase the dispersion of the catalytically active species, which is iron in this case. In addition to this, catalytic materials also typically require mechanical and thermal

stability.[61] Considering the iron species in the samples, no CT bands should be present beyond the 200-300 nm range in the UV-vis spectra of the samples. Additionally, a white or off-white powder color is expected. This is with the hope of achieving single-site iron as the only iron species in the catalyst.

With a molar ratio Fe:Si ≤ 0.025, the white and off-white gels made with acetate and dichloride achieve a loading up to 2.5 wt% Fe, whereas sulfate and trichloride achieve up to 2.1 wt% Fe. *iCP-0.025(III)-Cl* has a loading of 3.1 wt% Fe, but is also more beige, so this is likely because of a loss of silicon in the ion exchange and in turn higher Fe:Si molar ratios for the entire iCP trichloride series.

For these gel samples (Fe:Si ≤ 0.025), the LMCT bands at wavelengths below 300 nm are the dominating feature of the UV-vis spectra. There is also a striking resemblance with the spectrum of the Fe-modified amorphous silicate (Fig. (2.12)) by Tuel et al.[26] This is the region in which isolated iron is reported to appear, hence the appearance of the absorption bands imply the presence of iron in single-sites. In addition, the light color of these samples also suggest little presence of iron oxides. The only iron precursor which do not satisfy the criteria given for the UV-vis spectrum is iron dichloride, neither with nor without inert atmosphere. It is likely that this is solely because this precursor is, as it turned out, the only precursor with Fe(II). As suggested before, it is possible that ferrous ions have a harder time incorporating into the silica network because they do not form stable silicate complexes.

Due to the noise in the UV-spectra, it is somewhat difficult to accurately establish where the band positions are located. This makes it more challenging to attribute tetrahedral or octahedral coordination to the apparent isolated iron single-sites, as both can appear over the near same region in the spectrum.[104] Nevertheless, as was shown

in Figure (4.19), there is a possible indication of isolated tetrahedral iron sites in the form of a weak series of d-d bands for all samples with molar ratio Fe:Si = 0.01 (except for the dichloride precursor). The appearance of these bands have often been connected with tetrahedral sites in zeolites.[26] Combined with the CT band location below 300 nm, this can be taken as a strong suggestion of tetrahedral coordination for the apparent iron sites in the samples. Based on earlier reports it also appears more likely that the single-sites have tetrahedral, or distorted tetrahedral, coordination.[24–26] However, López et al.[27] reported that iron formed octahedral complexes with the silanol groups on the surface of their gels. They also reported on the presence of iron sites in the silica framework, but the coordination of these were not specified. Also 3-coordinated surface sites have been reported, and can be considered as a possibility.[26] To properly confirm which coordination the iron has in the gel samples, a more powerful characterization tool such as XAS would be needed. Without this, tetrahedral iron single-sites are assumed based on the CT band and d-d band locations.

For the gels with Fe:Si $\leq$ 0.025, an increased porosity is also detected in the structure of the gels compared to that of plain silica aerogel. This increase appears larger in gels made with sulfate and chloride precursors, than in gels made with acetate precursor. It appears that the larger surface area, pore sizes and pore volume are a direct result of introducing iron into the synthesis. This can be due to more pores caused by a stiffening or distortion of the silica network, or the presence of iron species on the surface blocking further formation of siloxy bridges between the silica particles. These observations are in correlation with earlier reports on other TMI supported aerogels by Kristoffersen,[24] Håbrekke,[22] and Kristiansen et al.[20] In addition, all as-prepared, annealed and calcined gels made with molar ratio Fe:Si $\leq$ 0.025 were found to be amorphous by XRD. The structural criteria established for the gels therefore appear to be fulfilled for the samples

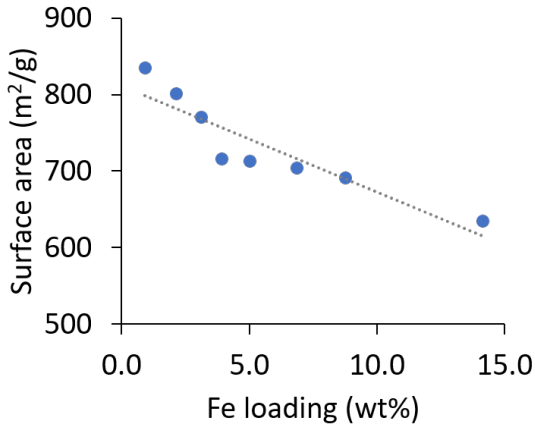

Figure 5.1: Variation of surface area with iron loading. The dotted line is a possible linear trend line.

with a low iron loading up to 2.5 wt%.

For samples made with a larger molar ratio (Fe:Si $\geq$ 0.05) the surface area and pore volume is lower than for samples with less iron. This decrease in surface area and pore volume can be seen in Figures (5.1) and (5.2), in which also possible trend lines have been inserted. There is more ambiguity as to what effect increasing iron content has on the pore sizes. For copper, larger amounts only led to larger pores,[20] but for cobalt and iron the average pore size has been reported to increase only to a certain loading before decreasing.[22,24] It is likely that the same trend is observed here, with the largest pores and average pore widths occurring in gels with a molar ratio Fe:Si = 0.05. An explanation for this is the likely formation of iron agglomerates or oxide particles in the pores or on the silica surface with increasing iron content in the samples. The darkening powder colors from beige to brown support this theory. The increasing amounts of iron oligomers

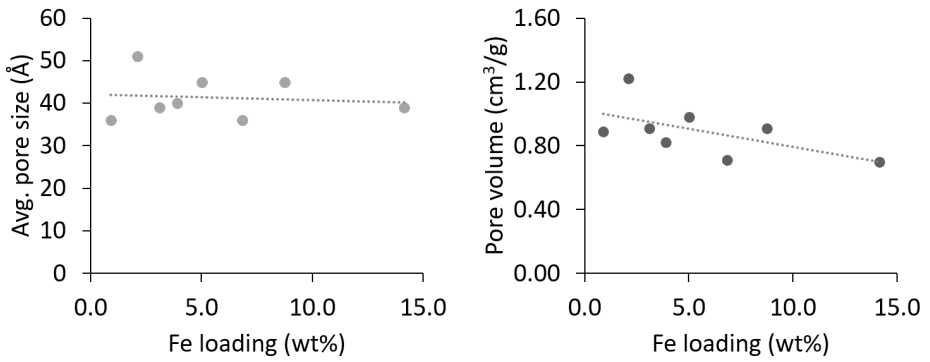

Figure 5.2: Variation of average pore size (left) and pore volume (right) with iron loading. The dotted lines are possible linear trend lines.

or oxide on the surface can lead to incomplete surface modification and in turn incomplete solvent exchange, as proposed by Kristiansen et al.[20] This has several repercussions: Because silanol groups are not exchanged for TMS groups, further condensation can occur and close off pores. Hydrophilic iron species and remaining silanol groups are also likely to create pockets of water, which during drying result in shrinkage and partly collapse of the framework. Molar ratios of Fe:Si ≥ 0.1 causes too much shrinkage, and the surface areas for these aerogel samples drop below the established limit at $700\,\mathrm{m^2\,g^{-1}}$. For as-prepared gels with larger amounts of iron (Fe:Si ≥ 5) with the sulfate precursor, also crystalline peaks appear in the diffractograms, thus failing to satisfy the criterion about amorphous structure.

The degree of incomplete surface modification is therefore a counter-effect to the stiffening or distortion possibly caused by iron in the silica matrix, and increases with more iron content in the samples. The presence of iron oxide can be supported by the darker sample colors, and from the UV-vis spectra, in which bands at higher wavelengths are

seen to grow more intense with increasing iron content. Because the XRD diffractograms show an absence of crystallinity in the samples, this can be attributed either to amorphous iron clusters or to nano-sized crystallites below the detection limit of the method. Both cases were reported by Fabrizioli et al.[25]

It has been reported before that the nature of iron also in zeolites is complicated.[10] As suggested by Brandenberger et al.,[108] the reason for this could be the similar energy of formation for the different iron containing species. It is therefore likely that especially the samples with molar ratios Fe:Si > 0.025 contain a variety of iron species, but that iron single-sites are still partially present. This can be inferred from the UV-vis spectra as well, since the band or bands in the 200-300 nm range appear to remain more or less consistent for all samples regardless of iron content. The same observation were made in the earlier studies on iron containing aerogel, and it has been proposed that iron is deposited on the surface only after the silica matrix becomes saturated.[25,27] The proposed saturation limit by López et al.[27] is as low as 0.5 wt% Fe. In spite of this, Fabrizioli et al.[25] reported on increasing uptake in the matrix until a maximum uptake at 7.0 wt% Fe (10 wt% Fe_2O_3) in the sample was reached, although the amount of other iron species were also increasing at the same time. No aerogels were reported to contain tetrahedral iron in the framework as the only iron species. This was also the case for Kristoffersen,[24] but a possible saturation limit was not addressed in his work. Based on these earlier reports and the current work, it seems likely that the loading must be kept as low as 2.5 wt% Fe or less in Fe-modified aerogels in order to prevent a variety of unwanted iron species to form, which is much lower than what has been achieved with copper (up to 11 wt% Cu).[20]

A possible reason for the low iron incorporation limit can be found by comparing with the successful copper single-site aerogel made by

Kristiansen et al.[20] In the case of copper, it was reported that copper tetrammine complexes played a significant role in the incorporation process at basic conditions. In contrast, iron does not form complexes with ammonia, but rather transforms into neutral hydroxo complexes at basic conditions, which then precipitate.[73] This could mean that before iron gets the chance to properly incorporate into the gel network, it is already being precipitated by the increasing pH caused by the addition of HMDS and the subsequent formation of ammonia in the solution. In agreement with this, Fabrizioli et al.[25] also implied that aqueous ammonia favored formation of small iron oxide particles. This can imply that the interaction between the guest metal and the base is an important factor for the stability of single-sites. It can also mean that iron is better incorporated under acidic conditions.

With heat treatment, it has been reported that iron migrate and aggregate into oxide nanoparticles, both in zeolites and in aerogels.[14–16,25] A strong indication of this is given by the tailing of the LMCT bands into the visible portion of the spectrum, an effect which only grows more pronounced with higher iron content.[25] The gel colors become more gray and darker after both annealing and calcination, which fits well with iron oxides having a dark color in general. Considering that no peaks show in the diffractograms of the annealed nor calcined samples, these oxides must either be amorphous or small enough to not be detected. Amorphous particles are highly unlikely after heat treatment, as amorphous nanoparticles have been reported to crystallize into the maghemite phase already at around 300 °C, before a full transition into the more stable hematite phase between 500-600 °C.[105] With this in mind, it is likely that crystallinity would have been detected in samples with molar ratios Fe:Si ≥ 0.05 if they had been calcined. Either way, with the increasing surface area and the steady pore sizes for the annealed samples compared with the as-prepared samples, the structural criteria are satisfied. For the calcined samples however, the

surface area drops.

To address the iron species again, the migrating species which form the oxide particles are not necessarily the iron single-sites in the framework, especially if iron species in the pores are already present. Previous reports have suggested the co-existence of several iron species after a heat treatment at 600 °C, including the presence of the isolated iron sites in the framework.[25,27] This can be supported by the UV-vis spectra. If this is the case, it means that iron single-sites in the framework potentially are more thermally stable, which is what is desired for the catalyst material. However, the broad absorption in the UV-vis spectra after calcination can also just be attributed to the iron oxide particles. In the end, the effect of heat treatment appears very similar to the effect of high iron content, as both appear to favor the formation of iron oxide. The difference being that increasing iron content causes formation of amorphous iron oxide particles, whereas both annealing at 450 °C and calcination at 700 °C also induces crystallization of the particles. There does not appear to be a difference related to the iron precursors in this regard.

The other important factor for catalyst carriers is the mechanical stability.[61] The aging process is reported to make the synthesized aerogels more robust by allowing more siloxane bridges to form and strengthening the interparticle necks.[3,53] Because of this, it is said to give decreased surface area and a shift towards larger pores, neither of which are notably observed for the gels prepared here compared with the surface areas and pore sizes as reported by Kristoffersen,[24] as well as with Håbrekke[22], Liu,[23] and Kristiansen et al.[20] Because a large surface area is desired, this is a good thing. It is likely that very little aging actually occurred in the gels as the surface modifying agents, which were added right before gelation, exchanged the silanol groups with TMS groups, thereby leaving few functional groups available for con-

densation in the long run. The SD method is probably better suited for aging of the gel for this reason. The mechanical stability of a catalyst material may be important for implementation, but the extended aging time given to the aerogels during synthesis in this work only seem to have lengthened the preparation time, and can most likely be cut short for the CP method.

All things considered, the best approach for making aerogel with iron in single-sites appears to be with low iron loadings, as to prevent the formation of other iron species in the pores. In this work, the samples with a molar ratio no larger than Fe:Si = 0.025 ($\leq$ 2.5 wt% Fe) best fulfill all the criteria set for the materials, although the thermal stability of the iron sites remains undetermined. As for the iron precursors, (oxidized) ferrous acetate, ferric chloride and ferric sulfate all appear more suitable for this synthesis than ferrous chloride. The best are therefore the acetate and trichloride precursors, as sulfate induces crystallinity at larger iron content (Fe:Si $>$ 5).

Chapter 6

Conclusions

Aerogel has successfully been synthesized from the inexpensive water-glass silica precursor using the more economical co-precursor method with ambient pressure drying.

Considering the incorporation of iron into the aerogel, low iron loadings no more than about 2.5 wt% Fe appeared necessary to incorporate iron only as single-sites in the silica matrix. This was not improved notably by using an inert atmosphere. It is difficult to properly confirm the coordination of the single-sites with UV-vis spectroscopy, but a tetrahedral coordination of the iron sites is not unlikely. Larger iron loadings seemed to cause the formation of amorphous iron oxide oligomers and nanoparticles instead of incorporating more iron into the silica framework as single-sites. The thermal stability of the Fe-modified gels is undetermined, as annealing at 450 °C possibly favored the formation and crystallization of iron oxide particles.

Between the iron precursors, (oxidized) ferrous acetate, ferric chloride and ferric sulfate were all suitable precursors for iron incorporation, however ferrous chloride appeared to favor the formation of iron oxide even at loadings below 2.5 wt% Fe. The best are therefore the acetate and trichloride precursors, as sulfate induced crystallinity in samples with larger precursor content, attributed to mascagnite crystals. Regarding the structure, the most porous gels were obtained with the sulfate precursor, whereas the least porous gels were obtained with the acetate precursor.

Compared with the plain silica aerogel, Fe-modified gels with a loading of 2.5 wt% Fe displayed increased surface area and porosity. This is probably caused by a distortion of the silica network when iron is incorporated. With larger iron loadings, the increasing porosity appeared to reach a threshold around 5 wt% Fe, where further introduction only resulted in reduction of porosity. This has been attributed to incomplete surface modification, and in turn shrinkage, due to the growing presence of iron oxide in the pores.

Chapter 7

Further Work

A more extensive spectroscopic study with XAS or a combination of other methods is necessary to accurately determine the iron species which are present in the gels. XAS characterization was cut from this work due to time restrictions and shutdown of the facility, but would most certainly have been beneficial. Other characterization methods can also be considered to gain better insight of the Fe-modified aerogels.

Catalytic testing is also needed. It remains to be seen if the Fe-modified aerogels are catalytically active for the methane conversion process, or other reactions in which iron have been used as a catalyst.

A study on the effects of heat treatment could also be done to investigate the thermal stability more thoroughly, possibly by TGA and XAS.

Further parameter studies on varying silica concentration or pH can be considered. It might be worth trying to incorporate iron under acidic conditions, and if this can provide larger iron incorporation in the silica network. Inert atmosphere can also be pursued further considering the possibility of increased porosity.

Bibliography

(1) Lewis, D. *Smithsonian* **2016**.

(2) Kistler, S. S. *Nature* **1931**, *127*, 741.

(3) Hüsing, N. et al. *Angewandte Chemie International Edition* **1998**, *37*, 22–45.

(4) Cao, G. et al., *Nanostructures and Nanomaterials: Synthesis, Properties and Applications*, 2nd ed.; World Scientific Publishing Co. Pte. Ltd.: 2011.

(5) Wright, J. D. et al., *Sol-Gel Materials: Chemistry and Applications*; CRC press: 2014.

(6) Schmidt, M. et al. *Journal of non-crystalline solids* **1998**, *225*, 364–368.

(7) Maleki, H. et al. *Applied Catalysis B: Environmental* **2018**, *221*, 530–555.

(8) Pajonk, G. *Catalysis Today* **1997**, *35*, 319–337.

(9) Rumble, J. R., *CRC Handbook of Chemistry and Physics*, 99th ed.; Taylor & Francis: 2018.

(10) Gao, F. et al. *ACS Catalysis* **2016**, *6*, 2939–2954.

(11) Sazinsky, M. H. et al. In *Sustaining life on planet earth: Metalloenzymes mastering dioxygen and other chewy gases*; Springer: 2015, pp 205–256.

(12) Guo, X. et al. *Science* **2014**, *344*, 616–619.

(13) Tang, P. et al. *Energy & Environmental Science* **2014**, *7*, 2580–2591.

(14) Hammond, C. et al. *Angewandte Chemie International Edition* **2012**, *51*, 5129–5133.

(15) Knops-Gerrits, P. et al. *Journal of Molecular Catalysis A: Chemical* **2001**, *166*, 135–145.

(16) Ribera, A. et al. *Journal of Catalysis* **2000**, *195*, 287–297.

(17) Otsuka, K. et al. *Studies in Surface Science and catalysis* **1998**, *119*, 15–24.

(18) Thomas, J. M. *Proceedings of The Royal Society A* **2012**, *468*, 1884–1903.

(19) Kristiansen, T. Aerogels; a new class of materials for catalytic purposes., Ph.D. Thesis, NTNU, Fakultet for naturvitenskap, 2013.

(20) Kristiansen, T. et al. *The Journal of Physical Chemistry C* **2011**, *115*, 19260–19268.

(21) Kristiansen, T. et al. *The Journal of Physical Chemistry C* **2014**, *118*, 2439–2453.

(22) Håbrekke, S. Introduction of Cobalt Into Silica Aerogels, Metal Speciation and Reducibility., MA thesis, NTNU, 2017.

(23) Liu, T. Functionalization of Silica Aerogels and AlPO-5 with Molybdenum, Rhenium-A Study on Metal Introduction Methods., MA thesis, NTNU, 2018.

(24) Kristoffersen, S. Incorporation of Iron (III) in Silica Aerogels., MA thesis, NTNU, 2016.

(25) Fabrizioli, P. et al. *Journal of Materials Chemistry* **2002**, *12*, 619–630.

(26) Tuel, A. et al. *Journal of the Chemical Society, Faraday Transactions* **1998**, *94*, 3501–3510.

(27) López, T. et al. *Materials chemistry and physics* **1992**, *30*, 161–167.

(28) Alemán, J. et al. *Pure and Applied Chemistry* **2007**, *79*, 1801–1829.

(29) Baumann, T. F. et al. *Chemistry of materials* **2005**, *17*, 395–401.

(30) Hammouda, L. B. et al. In *Aerogels Handbook*, Aegerter, M. A. et al., Eds.; Springer Science & Business Media: 2011; Chapter 6, pp 127–143.

(31) Hirashima, H. In *Aerogels Handbook*, Aegerter, M. A. et al., Eds.; Springer Science & Business Media: 2011; Chapter 7, pp 145–153.

(32) Li, J. et al. *Journal of Power Sources* **2006**, *158*, 784–788.

(33) Schubert, U. et al., *Synthesis of Inorganic Materials*; John Wiley & Sons: 2012.

(34) Anderson, A. M. et al. In *Aerogels Handbook*, Aegerter, M. A. et al., Eds.; Springer Science & Business Media: 2011; Chapter 3, pp 47–77.

(35) Warheit, D. B. *Journal of environmental pathology, toxicology and oncology* **2001**, *20*.

(36) Baetens, R. et al. *Energy and Buildings* **2011**, *43*, 761–769.

(37) Fesmire, J. E. *Cryogenics* **2006**, *46*, 111–117.

(38) Matias, T. et al. *Colloids and Surfaces A: Physicochemical and Engineering Aspects* **2015**, *480*, 260–269.

(39) Tsou, P. *Journal of Non-Crystalline Solids* **1995**, *186*, 415–427.

(40) Iijima, T. et al. *Nuclear Instruments and Methods in Physics Research Section A: Accelerators, Spectrometers, Detectors and Associated Equipment* **2000**, *453*, 321–325.

(41) Kim, G. S. et al. *Journal of the American Ceramic Society* **2001**, *84*, 453–55.

(42) Rao, A. V. et al. In *Aerogels Handbook*, Aegerter, M. A. et al., Eds.; Springer Science & Business Media: 2011; Chapter 5, pp 103–124.

(43) Dorcheh, A. S. et al. *Journal of materials processing technology* **2008**, *199*, 10–26.

(44) Rotter, H. et al. *Applied Catalysis B: Environmental* **2004**, *47*, 111–126.

(45) Engweiler, J. et al. *Applied Catalysis A: General* **1994**, *120*, 187–205.

(46) Osaki, T. et al. *Catalysis letters* **1998**, *52*, 171–180.

(47) Sánchez-Polo, M. et al. *Water research* **2006**, *40*, 3375–3384.

(48) Li, Y. et al. *Separation and Purification Technology* **2015**, *156*, 1035–1040.

(49) Einarsrud, M.-A. et al. *Journal of Non-Crystalline Solids* **1998**, *226*, 122–128.

(50) Bisson, A. et al. *Drying technology* **2003**, *21*, 593–628.

(51) Brinker, C. J. *Journal of Non-Crystalline Solids* **1988**, *100*, 31–50.

(52) Heinrich, T. et al. *Journal of Porous Materials* **1995**, *1*, 7–17.

(53) Iswar, S. et al. *Microporous and Mesoporous Materials* **2017**, *241*, 293–302.

(54) Hæreid, S. et al. *Journal of non-crystalline solids* **1995**, *185*, 221–226.

(55) Scherer, G. W. *Journal of Non-Crystalline Solids* **1988**, *100*, 77–92.

(56) Pierre, A. C. In *Aerogels Handbook*, Aegerter, M. A. et al., Eds.; Springer Science & Business Media: 2011; Chapter 1, pp 3–18.

(57) Gurav, J. L. et al. *Journal of Alloys and Compounds* **2009**, *471*, 296–302.

(58) Yokogawa, H. et al. *Journal of Non-Crystalline Solids* **1995**, *186*, 23–29.

(59) Rao, A. V. et al. *Journal of Non-Crystalline Solids* **2004**, *350*, 216–223.

(60) Bhagat, S. D. et al. *Solid State Sciences* **2007**, *9*, 628–635.

(61) Schwarz, J. A. et al. *Chemical Reviews* **1995**, *95*, 477–510.

(62) Owens, L. et al. *Journal of non-crystalline solids* **1995**, *186*, 177–183.

(63) Ma, Z. et al. *Fuel processing technology* **2007**, *88*, 29–33.

(64) Dunn, B. C. et al. *Applied Catalysis A: General* **2005**, *278*, 233–238.

(65) Zhu, J. et al. *Colloids and Surfaces A: Physicochemical and Engineering Aspects* **2009**, *342*, 97–101.

(66) Mayo, E. I. et al. *Inorganic chemistry* **2000**, *39*, 899–905.

(67) Mohanan, J. L. et al. *Chemistry of materials* **2003**, *15*, 2567–2576.

(68) Lai, S. et al. *Journal of molecular catalysis a: chemical* **2016**, *424*, 232–240.

(69) Pieterse, J. et al. *Applied Catalysis B: Environmental* **2004**, *51*, 215–228.

(70) Hall, W. K. et al. *Catalysis letters* **1998**, *52*, 13–19.

(71) Lehmann, G. *Physik der kondensierten Materie* **1971**, *13*, 297–306.

(72) Anthony, J. W. et al., *Handbook of Mineralogy*, 1st ed.; Mineral Data Publishing: 1990.

(73) Atkins, P. W. et al., *Inorganic chemistry*, 6th ed.; Oxford University Press: 2014; Chapter 8, 19.

(74) Magini, M. et al. *The Journal of Chemical Physics* **1979**, *71*, 4255–4262.

(75) Apted, M. et al. *Geochimica et Cosmochimica Acta* **1985**, *49*, 2081–2089.

(76) Persson, I. *Journal of solution chemistry* **2018**, *47*, 797–805.

(77) Schindler, P. et al. *Journal of Colloid and Interface Science* **1976**, *55*, 469–475.

(78) Weber Jr, W. et al. *Journal of Inorganic and Nuclear Chemistry* **1965**, *27*, 237–239.

(79) Jennings, J. R., *Catalytic ammonia synthesis: fundamentals and practice*; Springer Science & Business Media: 1991.

(80) Schulz, H. *Applied Catalysis A: General* **1999**, *186*, 3–12.

(81) Bols, M. L. et al. *Journal of the American Chemical Society* **2018**, *140*, 12021–12032.

(82) Tan, P. *Journal of Catalysis* **2016**, *338*, 21–29.

(83) Nozaki, C. et al. *Journal of the American Chemical Society* **2002**, *124*, 13194–13203.

(84) Ruitenbeek, M. et al. *Angewandte Chemie International Edition* **2014**, *53*, 11137–11139.

(85) Callister, W. D. et al., *Materials science and engineering, SI version*, 9th ed.; John Wiley & Sons NY: 2014, pp 103–108.

(86) Warren, B., *X-Ray Diffraction*; Dover Books on Physics; Dover Publications: 2012.

(87) Cullity, B. D. et al., *Elements of X-ray Diffraction*, 3rd ed.; Prentice-Hall: 2001, pp 101–102.

(88) Langmuir, I. *Journal of the American Chemical society* **1918**, *40*, 1361–1403.

(89) Davis, M. E. et al., *Fundamentals of chemical reaction engineering*; Courier Corporation: 2012.

(90) Sing, K. S. W. et al. *Pure and applied chemistry* **1985**, *57*, 603–619.

(91) Thommes, M. et al. *Pure and Applied Chemistry* **2015**, *87*, 1051–1069.

(92) Brunauer, S. et al. *Journal of the American chemical society* **1938**, *60*, 309–319.

(93) Roquerol, F. et al. *Academic Press, London* **1999**, *54*, 15893–15899.

(94) Salvador, F. et al. In *Studies in Surface Science and Catalysis*; Elsevier: 2002; Vol. 144, pp 379–386.

(95) Barrett, E. P. et al. *Journal of the American Chemical society* **1951**, *73*, 373–380.

(96) Bertier, P. et al. In *The Clay Minerals Society Workshop Lectures Series*, 2016; Vol. 21, pp 151–161.

(97) Thommes, M. *Chemie Ingenieur Technik* **2010**, *82*, 1059–1073.

(98) Scherer, G. W. et al. *Journal of non-crystalline solids* **1995**, *186*, 309–315.

(99) Miller, J. M., *Chromatography: concepts and contrasts*, 2nd ed.; John Wiley & Sons: 2009; Chapter 10.

(100) Gross, J. H., *Mass spectrometry: a textbook*, 1st ed.; Springer Science & Business Media: 2004; Chapter 1.

(101) Tippins, H. *Physical Review B* **1970**, *1*, 126.

(102) Kim, J. et al. *The Journal of Physical Chemistry C* **2013**, *117*, 986–993.

(103) Kumar, M. S. et al. *Journal of catalysis* **2004**, *227*, 384–397.

(104) Bordiga, S. et al. *Journal of Catalysis* **1996**, *158*, 486–501.

(105) Phu, N. et al. *Journal of Physics D: Applied Physics* **2011**, *44*, 345002.

(106) Fasiska, E. *Corrosion Science* **1967**, *7*, 833–839.

(107) Holleman, A. et al., *Inorganic Chemistry*; Academic Press: 2001.

(108) Brandenberger, S. et al. *Applied Catalysis A: General* **2010**, *373*, 168–175.

Appendices

Appendix A

Synthesis Parameters

Table A.1: Synthesis parameters for all the gel samples.

Sample name	Precursor molar ratios to Si				Fe precursor/
	H_2O	HMDS	HMDSO	Fe	Flask shape
CP-0.01(II)-Ac	30	1.1	1.0	0.01	Acetate
CP-0.025(II)-Ac	30	1.1	1.0	0.025	Acetate
CP-0.05(II)-Ac	30	1.1	1.0	0.05	Acetate
CP-0.1(II)-Ac	30	1.1	1.0	0.1	Acetate
iCP-0.01(II)-Ac	28	1.1	1.0	0.01	Acetate
iCP-0.025(II)-Ac	28	1.1	1.0	0.025	Acetate
iCP-0.05(II)-Ac	28	1.1	1.0	0.05	Acetate
CP-0.01(II)-Cl	32	1.1	1.0	0.01	Dichloride
CP-0.025(II)-Cl	32	1.1	1.0	0.025	Dichloride
CP-0.05(II)-Cl	32	1.1	1.0	0.05	Dichloride
CP-0.1(II)-Cl	32	1.1	1.0	0.1	Dichloride
iCP-0.01(II)-Cl	29	1.1	1.0	0.01	Dichloride
iCP-0.025(II)-Cl	29	1.1	1.0	0.025	Dichloride
iCP-0.05(II)-Cl	29	1.1	1.0	0.05	Dichloride
CP-0.01(III)-Cl	32	1.1	1.0	0.01	Trichloride
CP-0.025(III)-Cl	31	1.1	1.0	0.025	Trichloride
CP-0.05(III)-Cl	31	1.1	1.0	0.05	Trichloride
CP-0.1(III)-Cl	31	1.1	1.0	0.1	Trichloride
CP-0.2(III)-Cl	31	1.1	1.0	0.2	Trichloride
iCP-0.025(III)-Cl	23	1.1	1.0	0.025	Trichloride
iCP-0.05(III)-Cl	23	1.1	1.0	0.05	Trichloride
iCP-0.1(III)-Cl	23	1.1	1.0	0.1	Trichloride
CP-0.01(III)-Sulf	28	1.1	1.0	0.01	Sulfate
CP-0.025(III)-Sulf	28	1.1	1.0	0.025	Sulfate
CP-0.05(III)-Sulf	28	1.1	1.0	0.05	Sulfate
CP-0.1(III)-Sulf	28	1.1	1.0	0.1	Sulfate
iCP-0.01(III)-Sulf	33	1.1	1.0	0.01	Sulfate
iCP-0.025(III)-Sulf	33	1.1	1.0	0.025	Sulfate
iCP-0.05(III)-Sulf	33	1.1	1.0	0.05	Sulfate
iCP-round	42	0.80	0.83	0.025	Round flask
iCP-pear	42	0.80	0.83	0.025	Pear flask

Table A.2: Chemical compounds with formulas and names.

Formula	IUPAC name	Other name
C_7H_{16}	(n-)Heptane	
$Fe(C_2H_3O_2)_2$	Iron(II) acetate	Ferrous acetate
$FeCl_2 \cdot 4\,H_2O$	Iron(II) dichloride tetrahydrate	Ferrous chloride
$FeCl_3 \cdot 6\,H_2O$	Iron(III) trichloride hexahydrate	Ferric chloride
$Fe_2(SO_4)_3 \cdot XH_2O$	Iron(III) sulfate hydrate	Ferric sulfate
HF	Hydrofluoric acid	
HNO_3	Nitric acid	
$HN(Si(CH_3)_3)_2$	Hexamethyldisilizane	HMDS/ HMDZ
H_2O	Water	Water
H_4SiO_4	(Orto)silicic acid	
NaOH	Sodium hydroxide	
Na_2SiO_3	Sodium (meta)silicate	Waterglass
$(NH_4)_2SO_4$	Ammonium tetraoxosulfate	Mascagnite
$O(Si(CH_3)_3)_2$	Hexamethyldisiloxane	HMDSO
SiO_2	Silicon dioxide	Silica

Appendix B

Additional Plots and Tables

B.1 XRD Diffractograms

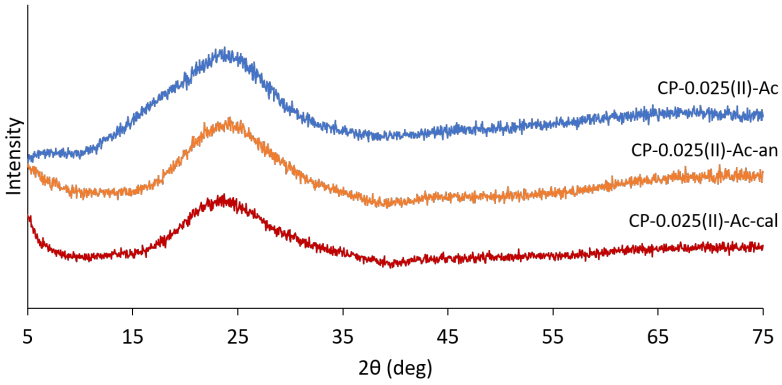

Figure B.1: XRD diffractograms of a sample after annealing at 450 °C and calcination at 700 °C, showing it is still amorphous.

B.2 BET and BJH Data

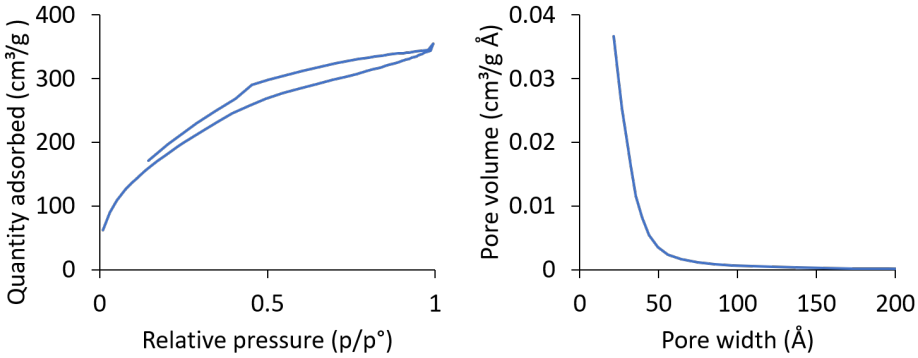

Figure B.2: Isotherm and PSD for the plain silica aerogel sample.

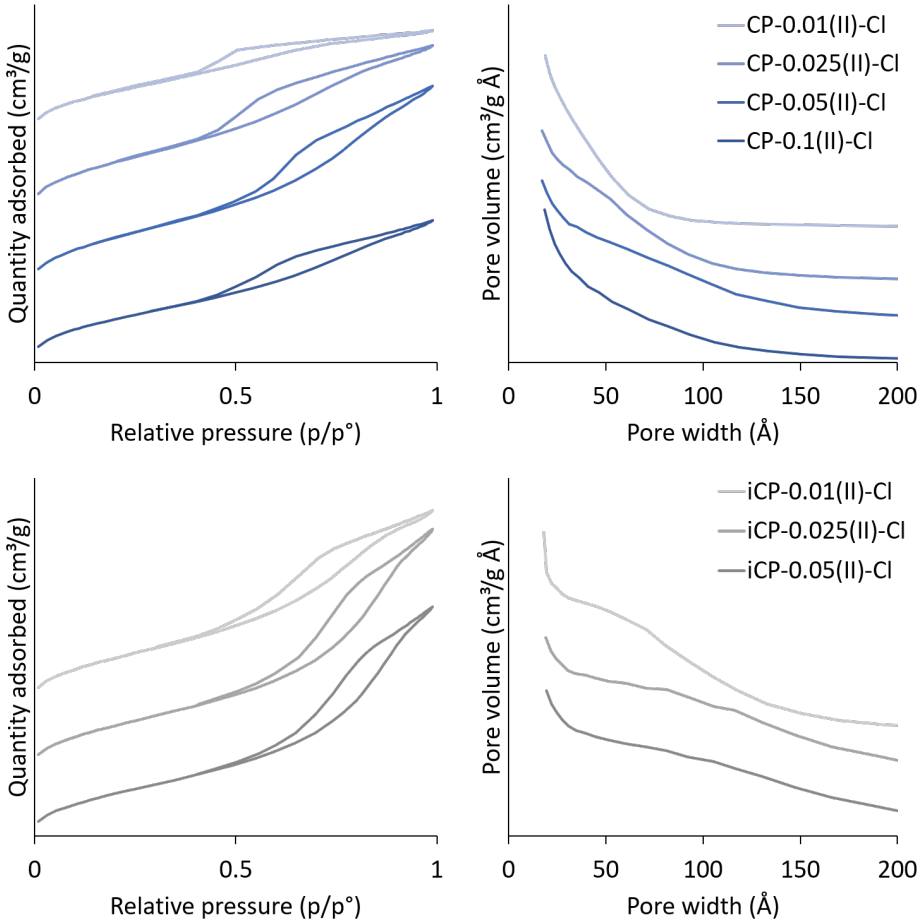

Figure B.3: Isotherms and PSD for the dichloride series.

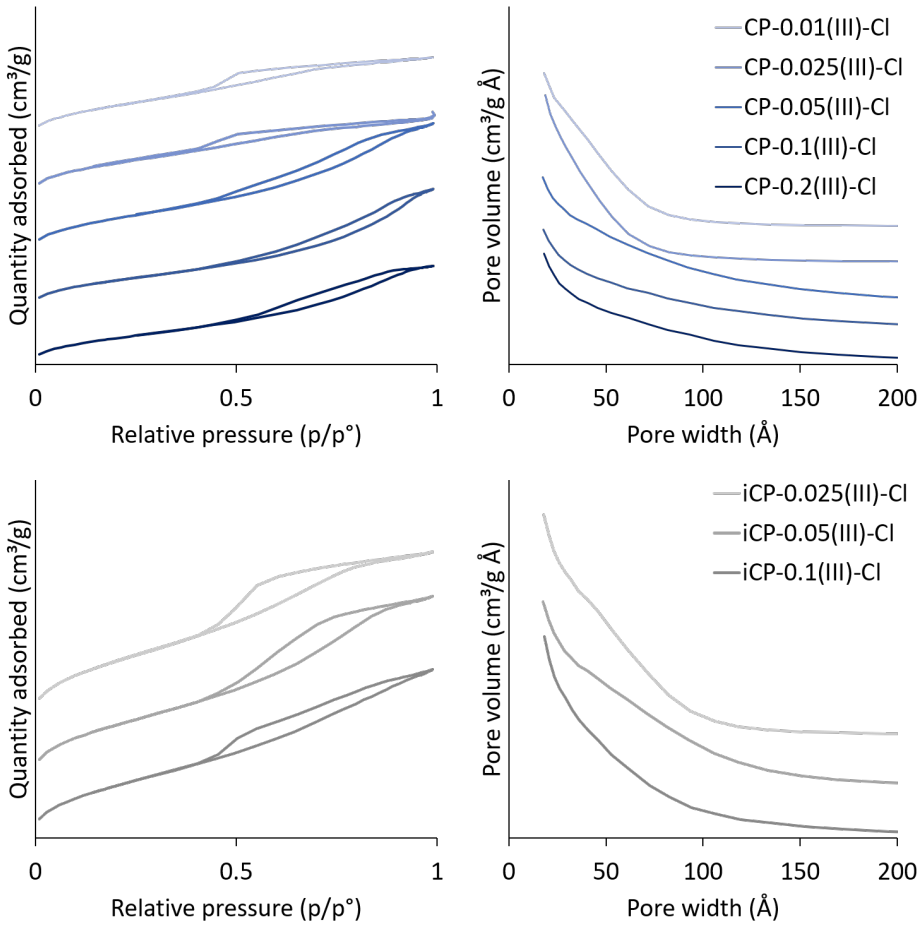

Figure B.4: Isotherms and PSD for the trichloride series.

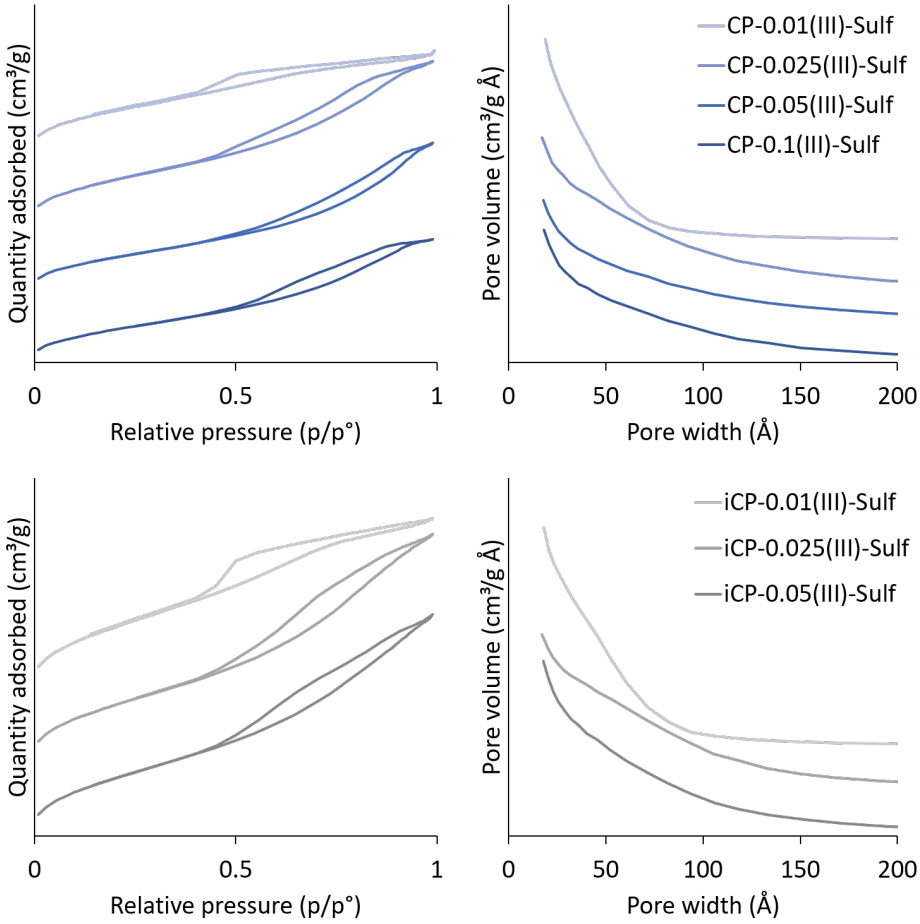

Figure B.5: Isotherms and PSD for the sulfate series.

Table B.1: BET surface area (S_{BET}), cumulative pore volume (V_p) and average pore width ($\overline{D}_p$) for the as-prepared and annealed samples.

Sample	S_{BET} (cm^2 g^{-1})		V_p (cm^3 g^{-1})		$\overline{D}_p$ (Å)	
	as-prep	an	as-prep	an	as-prep	an
CP-plain	714	-	0.62	-	34	-
CP-0.01(II)-Ac	745	897	0.72	0.60	35	32
CP-0.025(II)-Ac	774	843	0.83	0.66	37	35
CP-0.05(II)-Ac	715	737	0.85	0.67	40	39
CP-0.1(II)-Ac	577	614	0.61	0.55	38	38
iCP-0.01(II)-Ac	717	933	0.67	0.60	34	31
iCP-0.025(II)-Ac	790	865	0.82	0.64	36	35
iCP-0.05(II)-Ac	745	769	0.94	0.86	43	44
CP-0.01(II)-Cl	639	724	0.66	0.58	36	34
CP-0.025(II)-Cl	749	889	1.02	1.05	44	44
CP-0.05(II)-Cl	762	795	1.24	1.12	52	52
CP-0.1(II)-Cl	666	862	0.90	1.04	46	46
iCP-0.01(II)-Cl	801	914	1.30	1.45	57	54
iCP-0.025(II)-Cl	792	934	1.64	1.74	71	66
iCP-0.05(II)-Cl	766	828	1.57	1.64	72	70
CP-0.01(III)-Cl	835	792	0.89	0.76	36	36
CP-0.025(III)-Cl	802	761	1.22	1.02	51	51
CP-0.05(III)-Cl	716	700	0.82	0.73	40	41
CP-0.1(III)-Cl	704	760	0.71	0.72	36	37
CP-0.2(III)-Cl	635	753	0.70	0.77	39	39
iCP-0.025(III)-Cl	771	828	0.91	0.86	39	40
iCP-0.05(III)-Cl	713	759	0.98	0.93	45	46
iCP-0.1(III)-Cl	692	693	0.91	0.83	45	45
CP-0.01(III)-Sulf	829	870	0.90	0.68	38	34
CP-0.025(III)-Sulf	888	967	1.41	1.28	51	51
CP-0.05(III)-Sulf	739	785	1.31	1.19	59	58
CP-0.1(III)-Sulf	724	643	1.10	0.89	51	51
iCP-0.01(III)-Sulf	812	947	0.92	0.94	38	38
iCP-0.025(III)-Sulf	759	888	1.21	1.17	51	51
iCP-0.05(III)-Sulf	770	886	1.18	1.17	51	51

B.3 ICP-MS Data

Table B.2: Experimental content of iron in the samples as determined by ICP-MS.

Sample name	Fe loading (wt%)		Exp. Fe:Si	
	as-prep	an	as-prep	an
CP-0.01(III)-Cl	0.91	-	0.017	-
CP-0.025(III)-Cl	2.12	2.11	0.030	0.025
CP-0.05(III)-Cl	3.91	-	0.084	-
CP-0.1(III)-Cl	6.84	-	0.144	-
CP-0.2(III)-Cl	14.15	-	0.305	-
iCP-0.025(III)-Cl	3.12	3.43	0.051	0.040
iCP-0.05(III)-Cl	5.01	-	0.109	-
iCP-0.1(III)-Cl	8.74	-	0.199	-
CP-0.025(II)-Ac	2.40	2.46	0.037	0.026
iCP-0.025(II)-Ac	2.17	2.17	0.035	0.027
CP-0.025(II)-Cl	2.46	2.40	0.034	0.025
iCP-0.025(II)-Cl	2.24	2.31	0.035	0.024
CP-0.025(III)-Sulf	1.89	1.95	0.030	0.021
iCP-0.025(III)-Sulf	1.93	2.07	0.031	0.022

B.4 UV-Vis Spectra

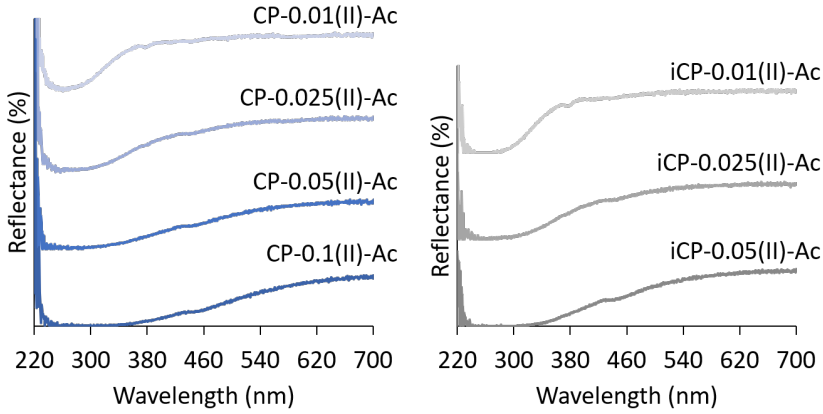

Figure B.6: UV-vis spectra for the acetate series.

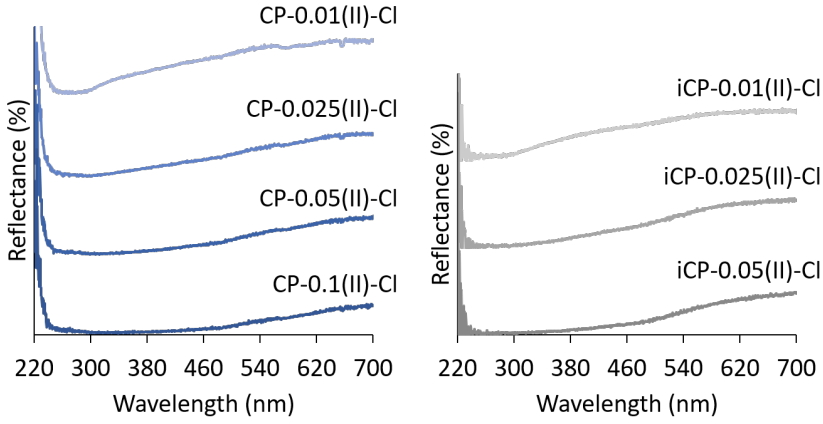

Figure B.7: UV-vis spectra for the dichloride series.

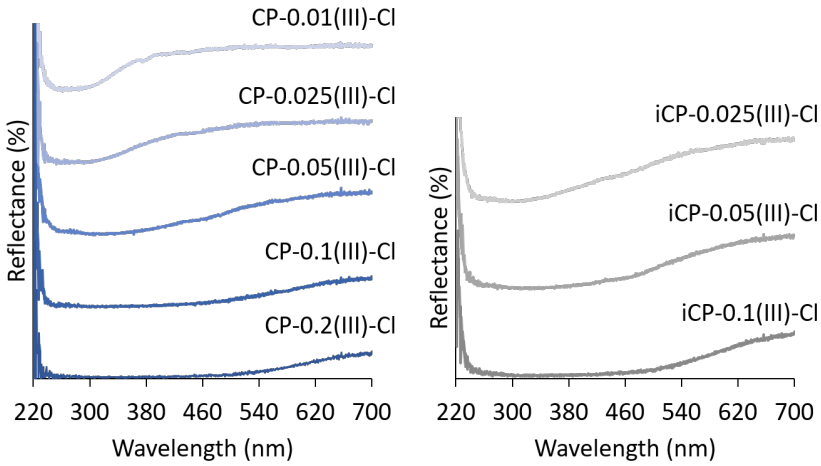

Figure B.8: UV-vis spectra for the trichloride series.

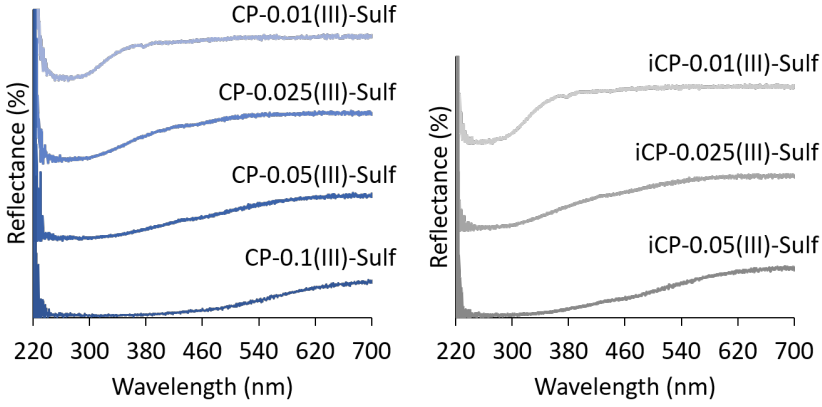

Figure B.9: UV-vis spectra for the sulfate series.

Gaute Holst Aasland

Synthesis of Silica Aerogels with Single-Site Iron for Heterogeneous Catalysis

NTNU
Kunnskap for en bedre verden